Petroleum Science 21 (2024) 4034–4051

Contents lists available at ScienceDirect

Petroleum Science

journal homepage: www.keaipublishing.com/en/journals/petroleum-science

Original Paper

Radiation efficiency and energy distribution from a borehole dipole source in the vertical transverse isotropic formation

Xi-Hao Gu [a, d], Fan-Tong Kong [c], Yuan-Da Su [a, b], Xiao-Ming Tang [a, b, *]

[a] School of Geosciences, China University of Petroleum (East China), Qingdao, 266580, Shandong, China
[b] Laoshan Laboratory, Qingdao, 266580, Shandong, China
[c] Ocean College, Jiangsu University of Science and Technology, Zhenjiang, 212100, Jiangsu, China
[d] Centre for Exploration Geophysics, Curtin University, Perth, 6845, Australia

ARTICLE INFO

Article history:
Received 25 August 2023
Received in revised form
2 July 2024
Accepted 5 September 2024
Available online 6 September 2024

Edited by Jie Hao and Min Li

Keywords:
Dipole source
Shear-wave reflection survey
Anisotropic formation
Energy flux
Radiation efficiency

ABSTRACT

Dipole Shear-Wave Reflection Survey (DSRS) has gained wide application in identifying unconventional reservoirs in anisotropic formations. Previous investigations have illuminated how boreholes complicate the distribution of acoustic energy. However, these models have not accounted for the anisotropic context, rendering them insufficient for analyzing acoustic energy distribution and radiation efficiency in anisotropic formations. We derive expressions for energy flux and radiation efficiency from a borehole dipole source in the vertical-transverse isotropic (VTI) media using the Umov-Poynting vector and steepest-descent solution. Utilizing this approach, we systematically evaluate the sensitivity of anisotropic parameters to energy flux and radiation efficiency, unveiling intricate variations of these properties across frequency and anisotropic parameters. Our findings emphasize the substantial influence of formation anisotropy on energy distribution from a dipole source inside the borehole. Due to energy conversion between wave modes, five radiation wave modes are elicited by the dipole source, with the SH wave retaining its status as the prime candidate for DSRS in fast formations owing to its elevated radiation efficiency. Conversely, the qP-qP wave exhibits advantages over S waves in unconsolidated formations. A key distinction between isotropic and anisotropic media is the presence of dominant excitation frequencies in the low-frequency domain. The significance of dominant excitation-frequency bands is validated by field data, emphasizing their pivotal role. These results offer valuable insights for designing DSRS measurement strategies, which have broad application expectations for unconventional oil and gas exploration.

1. Introduction

Dipole Shear-Wave Reflection Survey (DSRS) has emerged as a widely employed borehole exploration technology capable of identifying and locating hydrocarbon reservoirs (Tang and Patterson, 2009; Li et al., 2021). Borehole dipole sources generate elastic waves that propagate through the deep underground and enable obtaining high-resolution images of subsurface structures surrounding the borehole (Lee et al., 2019; Xu et al., 2021). In comparison to the traditional monopole acoustic reflection imaging method (Wang et al., 2015; Hirabayashi and Leaney, 2019), DSRS offers several advantages, including deeper penetration and orientational sensitivity (Tang et al., 2008; Cheng et al., 2023; Hei et al., 2023). However, it is noteworthy to mention that the reflection waves used for imaging are considerably weaker than the predominant borehole direct signals (Ji et al., 2021; Kong et al., 2023; Zhao et al., 2023). Moreover, the presence of an anisotropic formation environment, particularly the vertical-transverse isotropic (VTI) formation commonly encountered when drilling in unconventional formations (Fang et al., 2014; Han et al., 2020), complicates the distribution of borehole acoustic energy and adversely affects the extraction of weak reflected signals (Liu et al., 2019; Gu et al., 2021). Enhancing the ability of dipole sources to illuminate geologic bodies located away from the borehole in the VTI environment, enabling the detection of deeper structures and achieving clearer imaging (Tang et al., 2024), requires an effective

* Corresponding author. School of Geosciences, China University of Petroleum (East China), Qingdao, 266580, Shandong, China.
E-mail address: tangxiam@aliyun.com (X.-M. Tang).

https://doi.org/10.1016/j.petsci.2024.09.006

approach to calculate the dominant frequency band and optimize the excitation performance.

The distribution of borehole acoustic energy plays a critical role in borehole acoustic studies. Winbow (1991) introduces the concept of radiation efficiency which represents the ratio of radiation energy flux to guided wave energy flux, enabling the assessment of the capability of a borehole source to radiate elastic energy into the surrounding formation. Cao et al. (2016) calculate the radiation energy fluxes and efficiencies of different borehole acoustic sources, demonstrating that the dipole source is more beneficial for imaging measurement than the monopole source. Subsequent investigations have detailed the energy fluxes and efficiencies of dipole radiant waves in various scenarios (Li et al., 2022), including wireline, logging while drilling (Wei et al., 2019), and casing (Tang et al., 2019) cases. These studies validated that the SH wave is the optimal candidate for reflection surveys, and determining the dominant excitation-frequency band is crucial for improving the reflection signal-to-noise ratio. However, previous studies assume isotropic media surrounding the borehole, which does not accurately model laminated formations in reality. With respect to the dipole source in a borehole among layered formations, often characterized as VTI media, researchers focused on estimating the shear velocity (He and Hu, 2009; Zeng and Li, 2022) and extracting the shear anisotropic parameters (Thomsen, 1986; Xu et al., 2017) using borehole mode wave. Only recently have there been efforts to model and analyze dipole radiation and reflection wavefields in VTI formation. For instance, Li et al. (2017) evaluate a 3D finite-difference method to model the dipole radiation and reflection waves in VTI formation. To enhance computing efficiency, Gu et al. (2023) develop an analytical method based on the steepest-descent solution to model DSRS for VTI formation, revealing the strong sensitivity of radiation and reflection wavefields to the existence of formation anisotropy. Nevertheless, the impact of formation anisotropy on the energy distribution from a borehole dipole source has not been analyzed in previous works.

This study put forward an effective approach to calculate energy fluxes and radiation efficiencies and analyze the influence of formation anisotropy on acoustic energy distribution, which serves as a crucial step in designing the excitation frequency band for DSRS in VTI formation. Specifically, we consider a dipole source positioned in a borehole surrounded by VTI media, and derive the expressions for energy flux and radiation efficiency using the Umov-Poynting vector and steepest-descent solution. To validate our proposed solution, we conduct a comparative analysis between the anisotropic results and the previous isotropic results obtained from an isotropic model. Moreover, we perform a comprehensive assessment of the sensitivity of anisotropic parameters to energy flux and radiation efficiency, presenting detailed variations of these properties concerning frequency and anisotropic parameters. Notably, we thoroughly discuss the dominant excitation-frequency band and the emergence of low-frequency peaks in anisotropic media. We close by comparing imaging results obtained from different frequency bands in an anisotropic formation with those from an isotropic formation, along with proving the validity of our results.

2. Theory and method

2.1. Energy fluxes of borehole guided waves in VTI formation

In the context depicted in Fig. 1, wherein a dipole source parallel to the x-axis and positioned within a borehole of radius a is excited, the ensuing elastic waves can be classified into two distinct categories contingent upon their propagation direction. The first group

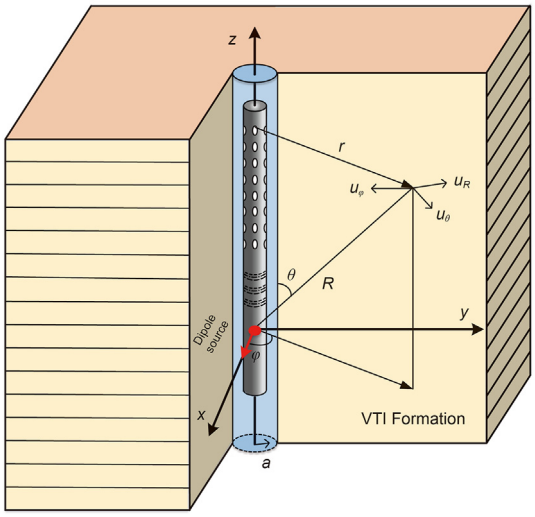

Fig. 1. The VTI model for analyzing radiation efficiency and energy distribution from a borehole dipole source.

encompasses flexural waves, primarily localized within the borehole, propagating along its axis. When captured by dipole receivers, these waves yield well-recognized acoustic full waveform array logs. The second group embodies elastic energy emanating beyond the confines of the borehole, penetrating the surrounding formation. This ensemble encompasses the SH wave as well as two coupled quasi-P (qP) and quasi-SV (qSV) waves (Dong and Toksöz, 1995).

In Logging While Drilling (LWD) measurements, the impact of the drill collar on acoustic energy distribution must be considered, given that the instrument occupies a substantial portion of the borehole. Conversely, wireline logging measurements involve a notably smaller tool size than in LWD scenarios. Practically, the transmitting and receiving components of the logging instrument in wireline setups feature notches, and the steel casing is thin, and connected by soft materials such as rubber. Consequently, this leads to a significantly diminished impact of the tool body on field wireline measurements, with no discernible presence of instrument waves in the waveforms recorded during wireline logging. As a result, this study concentrates on the pronounced influence of formation anisotropy on borehole dipole source energy distribution, excluding consideration of the influence of the tool body.

Energy-flux density is a crucial quantity that describes a wavefield, representing the energy carried by elastic waves across a unit area perpendicular to the velocity direction. Energy flux encapsulates the complete energy traversing a designated surface, attainable through integration of the energy-flux density across that surface. In the context of a dipole source, it generates the most fundamental lowest-order flexural wave, releasing energy along the borehole within the logging frequency band. Calculating the energy-flux vector requires determining the radial, axial, and azimuthal Umov-Poynting vector components for the flexural wave. The energy-flux density is able to be calculated solely by employing the axial energy-flux vector, as it represents the component of the average energy-flux vector aligned with the direction of wave propagation. Energy-flux densities of flexural waves consist of two components: the borehole fluid component, denoted as E_f, and the VTI formation component, designated as E_{fm}. In a cylindrical coordinate framework (r, φ, z), they can be written as:

$$\begin{cases} E_{\mathrm{f}}|_{r<a} = -\dfrac{1}{2}\mathrm{Re}\left(P_{\mathrm{f}} \cdot v_{\mathrm{fz}}^{*}\right) \\ E_{\mathrm{fm}}|_{r>a} = -\dfrac{1}{2}\mathrm{Re}\left(\sigma_{rz} \cdot v_{r}^{*} + \sigma_{\varphi z} \cdot v_{\varphi}^{*} + \sigma_{zz} \cdot v_{z}^{*}\right) \end{cases} \tag{1}$$

where P_{f} and v_{fz}^{*} are the fluid pressures and complex conjugates of particle velocities along z-axis in the borehole fluid, respectively; v_{r}^{*}, v_{φ}^{*} and v_{z}^{*} are the complex conjugates of radial, azimuthal and axial particle velocities in the infinite formation, respectively. σ_{rz}, $\sigma_{\varphi z}$ and σ_{zz} are the axial stresses in the formation. Re means to take the real part of the corresponding complex number. The detailed expressions of the fluid pressures, the stresses and the particle-velocity components in Eq. (1) are derived as follows.

In accordance with the Helmholtz theorem, the displacement in the borehole fluid $\mathbf{u}_{\mathrm{f}}$ and elastic solid $\mathbf{u}_{\mathrm{s}}$ can be given with regard to their potentials, respectively, as

$$\begin{cases} \mathbf{u}_{\mathrm{f}} = \nabla\phi_{\mathrm{f}} \\ \mathbf{u}_{\mathrm{s}} = \nabla\phi + \nabla \times (\chi\widehat{\mathbf{z}})\phi + \nabla \times \nabla \times (\Gamma\widehat{\mathbf{z}}) \end{cases} \tag{2}$$

Here, $\widehat{\mathbf{z}}$ signifies a unit vector in the borehole direction, ϕ_{f} depicts the acoustic wave displacement potential inside borehole fluid, and ϕ, χ and Γ depict the qP, SH and qSV wave displacement potentials in the VTI formation, separately. Suitable expressions for the displacement potentials are (Tang and Cheng, 2004)

$$\begin{cases} \phi_{\mathrm{f}} = \dfrac{1}{n!}\left(\dfrac{fr_0}{2}\right)^{n}\dfrac{\sin(n\varphi)}{4\pi^2}S(\omega)\displaystyle\int_{-\infty}^{+\infty} A_n(\omega,k)I_n\left(q_{\mathrm{f}}r\right)e^{\mathrm{i}kz}\mathrm{d}k \\ \phi = \dfrac{1}{n!}\left(\dfrac{fr_0}{2}\right)^{n}\dfrac{\sin(n\varphi)}{4\pi^2}S(\omega)\displaystyle\int_{-\infty}^{+\infty} (B_n(\omega,k)K_n(q_{\mathrm{P}}r) + b'F_n(\omega,k)K_n(q_{\mathrm{SV}}r))e^{\mathrm{i}kz}\mathrm{d}k \\ \chi = \dfrac{1}{n!}\left(\dfrac{fr_0}{2}\right)^{n}\dfrac{\cos(n\varphi)}{4\pi^2}S(\omega)\displaystyle\int_{-\infty}^{+\infty} D_n(\omega,k)K_n(q_{\mathrm{SH}}r)e^{\mathrm{i}kz}\mathrm{d}k \\ \Gamma = \dfrac{1}{n!}\left(\dfrac{fr_0}{2}\right)^{n}\dfrac{\sin(n\varphi)}{4\pi^2}S(\omega)\displaystyle\int_{-\infty}^{+\infty} (a'B_n(\omega,k)K_n(q_{\mathrm{P}}r) + F_n(\omega,k)K_n(q_{\mathrm{SV}}r))e^{\mathrm{i}kz}\mathrm{d}k \end{cases} \tag{3}$$

$$\begin{cases} u_{\mathrm{fz}} = \mathrm{i}kA_nI_n\left(q_{\mathrm{f}}r\right)e^{\mathrm{i}kz}\sin(n\varphi) \\ u_r = \left\{\begin{array}{l}(\mathrm{i}k + b')F_n(nK_n(q_{\mathrm{SV}}r)/r - q_{\mathrm{SV}}K_{n+1}(q_{\mathrm{SV}}r)) + \\ (\mathrm{i}ka' + 1)B_n(nK_n(q_{\mathrm{P}}r)/r - q_{\mathrm{P}}K_{n+1}(q_{\mathrm{P}}r)) + nD_nK_n(q_{\mathrm{SH}}r)/r\end{array}\right\}e^{\mathrm{i}kz}\sin(n\varphi) \\ u_{\varphi} = \left\{\begin{array}{l}D_n(nK_n(q_{\mathrm{SH}}r)/r - q_{\mathrm{SH}}K_{n+1}(q_{\mathrm{SH}}r)) + \\ [n(\mathrm{i}k + b')F_nK_n(q_{\mathrm{SV}}r)/r + n(\mathrm{i}ka' + 1)B_nK_n(q_{\mathrm{P}}r)/r]\end{array}\right\}e^{\mathrm{i}kz}\cos(n\varphi) \\ u_z = \left[\left(\mathrm{i}kb' - q_{\mathrm{SV}}^2\right)F_nK_n(q_{\mathrm{SV}}r) + \left(-a'q_{\mathrm{P}}^2 + \mathrm{i}k\right)B_nK_n(q_{\mathrm{P}}r)\right]e^{\mathrm{i}kz}\sin(n\varphi) \end{cases} \tag{6}$$

Here r_0 denotes the radius of the dipole source, $S(\omega)$ denotes the frequency spectrum of dipole source. f and q denote, separately, the radial wavenumbers of the fluid and formation, and subscripts SH, P and SV denote an SH wave and coupled qP and qSV waves. K_n is the n-order modified Bessel function related to outgoing wave, with $n = 1$ denoting the dipole (the analytical solutions obtained in this paper can be applied to monopole or high-pole modes by taking different values for n in the equations, such as $n = 2$ denoting the quadrupole). Elements a' and b' are given in the following

$$\begin{cases} a' = -\dfrac{1}{\mathrm{i}k}\dfrac{(c_{13}+2c_{44})k^2 - c_{11}q_{\mathrm{P}}^2 - \rho\omega^2}{c_{44}k^2 - (c_{11}-c_{13}-c_{44})q_{\mathrm{P}}^2 - \rho\omega^2} \\ b' = -\mathrm{i}k\dfrac{c_{44}k^2 - (c_{11}-c_{13}-c_{44})q_{\mathrm{SV}}^2 - \rho\omega^2}{(c_{13}+2c_{44})k^2 - c_{11}q_{\mathrm{SV}}^2 - \rho\omega^2} \end{cases} \tag{4}$$

A common equation for obtaining the unknown amplitude coefficients B_n, D_n and F_n is built considering the boundary condition at borehole wall

$$\begin{bmatrix} N_{11} & N_{12} & N_{13} & N_{14} \\ N_{21} & N_{22} & N_{23} & N_{24} \\ N_{31} & N_{32} & N_{33} & N_{34} \\ N_{41} & N_{42} & N_{43} & N_{44} \end{bmatrix}\begin{bmatrix} A_n \\ B_n \\ D_n \\ F_n \end{bmatrix} = \begin{bmatrix} b_1 \\ b_2 \\ b_3 \\ b_4 \end{bmatrix}. \tag{5}$$

where A_n is the unknown coefficient of borehole wave. b_i and N_{ij} $(i,j = 1,2,3,4)$ are expressed in Appendix A.

Substituting the potentials of Eq. (3) into Eq. (2), we obtain the expression of radial displacement in fluid and radial, azimuthal and axial displacement in VTI formation

For the purpose of obtaining the pressure P_{f} and particle velocity V_{fz} in the borehole fluid, the potential ϕ_{f} and displacement u_{fz} are substituted into the pressure-potential relation $P_{\mathrm{f}} = \rho\omega^2\phi_{\mathrm{f}}$ and velocity-displacement relation $v_{\mathrm{fz}} = \mathrm{i}\omega u_{\mathrm{fz}}$ yield

$$\begin{cases} P_{\mathrm{f}} = \rho\omega^2 A_n(\omega,k) I_n\left(q_{\mathrm{f}} r\right) e^{\mathrm{i}kz} \sin(n\varphi) \\ V_{\mathrm{fz}} = -\omega k A_n I_n\left(q_{\mathrm{f}} r\right) e^{\mathrm{i}kz} \sin(n\varphi) \end{cases} \tag{7}$$

The radial, azimuthal and axial particle velocities in the infinite formation also can be obtained by substituting the displacements u_{r}, u_{φ} and u_z into velocity-displacement relation. Employing Eq. (6) in the strain-displacement relation in cylindrical coordinate system, the stress components outlined in Eq. (1) are obtained through Hooke's law:

$$\begin{cases} \sigma_{rz} = \left\{ \begin{array}{l} F_n\left(k^2 + q_{\mathrm{SV}}^2 - \mathrm{i}2kb'\right)\left(q_{\mathrm{SV}} K_{n+1}(q_{\mathrm{SV}} r) - nK_n(q_{\mathrm{SV}} r)/r\right) + \\ B_n\left(a'k^2 + a' q_{\mathrm{P}}^2 - \mathrm{i}2k\right)\left(q_{\mathrm{P}} K_{n+1}(q_{\mathrm{P}} r) - nK_n(q_{\mathrm{P}} r)/r\right) + \mathrm{i}nkD_n K_n(q_{\mathrm{SH}} r)\Big/ r \end{array} \right\} \sin(n\varphi) c_{44} e^{\mathrm{i}kz} \\ \sigma_{\varphi z} = \left\{ \begin{array}{l} ikD_n\left(q_{\mathrm{SH}} K_{n+1}(q_{\mathrm{SH}} r) - nK_n(q_{\mathrm{SH}} r)/r\right) + \\ \left[\left(\mathrm{i}2kb' - k^2 - q_{\mathrm{SV}}^2\right) nF_n K_n(q_{\mathrm{SV}} r)\Big/ r + \left(\mathrm{i}2k - a'k^2 - a' q_{\mathrm{P}}^2\right) nB_n K_n(q_{\mathrm{P}} r)\Big/ r\right] \end{array} \right\} \cos(n\varphi) c_{44} e^{\mathrm{i}kz} \\ \sigma_{zz} = \left\{ \begin{array}{l} \left[-k^2 c_{33} b' + \mathrm{i}(c_{13} - c_{33}) q_{\mathrm{SV}}^2 k + c_{13} q_{\mathrm{SV}}^2 b' \right] F_n K_n(q_{\mathrm{SV}} r) + \\ \left[-k^2 c_{33} + \mathrm{i}(c_{13} - c_{33}) a' q_{\mathrm{P}}^2 k + c_{13} q_{\mathrm{P}}^2 \right] B_n K_n(q_{\mathrm{P}} r) \end{array} \right\} \sin(n\varphi) e^{\mathrm{i}kz} \end{cases} \tag{8}$$

The determinant of N_{ij} results in a dispersion equation governing guided waves for the VTI formation

$$G(k,\omega) = \det \begin{pmatrix} N_{11} & N_{12} & N_{13} & N_{14} \\ N_{21} & N_{22} & N_{23} & N_{24} \\ N_{31} & N_{32} & N_{33} & N_{34} \\ N_{41} & N_{42} & N_{43} & N_{44} \end{pmatrix} = 0 \tag{9}$$

where $\det(N_{ij})$ indicates the determinant of N_{ij}. Eq. (9) is known as the period or dispersion equation. When ω is held constant, this equation assumes a nonlinear form with respect to wavenumber k, necessitating a numerical solution.

For the particle velocities and stress components in Eqs. (1) and (8), we perform a k integration to obtain the wave excitations spectrum in the frequency domain. The poles of the dipole acoustic field correspond to the flexural mode. The straightforward wavenumber integration as described previously is along the real wavenumber axis. An alternative approach involves contour integration in a complex k plane based on Cauchy's theorem. For example, the excitation spectrum of particle velocity v_{fz} in the frequency domain may be written

$$\begin{aligned} v_{\mathrm{fz}}(\omega) = & \int_{-\infty}^{+\infty} v_{\mathrm{fz}}(\omega,k) \mathrm{e}^{\mathrm{i}kz} \mathrm{d}k \\ & = 2\pi \mathrm{i} \sum_{l} \mathrm{Res}\left[v_{\mathrm{fz}}(\omega,k) \mathrm{e}^{\mathrm{i}kz} \right]_{k_l} \end{aligned} \tag{10}$$

where Res indicates taking residue of $v_{\mathrm{fz}}(\omega,k)\mathrm{e}^{\mathrm{i}k\,z}$ at the wavenumber value k_l at the lth pole (Considering $l = 1$ associated with the first-order flexural wave in dipole logging frequency range). By substituting the aforementioned pressures, particle velocities, and strains into Eq. (1) to derive E_{f} and E_{fm}, followed by the integration of flux densities across a section encompassing the borehole fluid and VTI formation (note that the two media are separated by the borehole radius), the computation of the flexural wave energy flux along the borehole is realized in the following manner:

$$W_{\mathrm{gw}} = 2\pi \left(\int_0^a E_{\mathrm{f}} + \int_a^{\infty} E_{\mathrm{fm}} \right) r \mathrm{d}r \tag{11}$$

2.2. Energy fluxes of radiation waves in VTI formation

In the following, we proceed with the calculation of the radiation energy flux in spherical coordinate system (R, θ, φ). As a borehole source is excited, the radiated wave propagates outward into the formation as a spherical wave. The far-field displacements of qP, SH and qSV radiated waves from a dipole source can be determined by using the steepest descent method for VTI medium. We utilize the results of Gu et al. (2023) for a borehole dipole source embedded in VTI formation. The specific expressions for these waves are provided below.

With regard to qP wave:

$$\begin{cases} u_{R-\mathrm{p}} = \dfrac{S(\omega)}{n\,!}\left(\dfrac{fr_0}{2}\right)^n \dfrac{1}{4\pi\rho V_{\mathrm{P}}^2 R}\left[\rho V_{\mathrm{P}}^2\left(\dfrac{-q_{\mathrm{P0}}B_n(\omega,k_{\mathrm{P0}})}{\sqrt{q_{\mathrm{P0}}\sin\theta|w_{\mathrm{P}}''(k_{\mathrm{P0}})|}}\sin\theta + \dfrac{\mathrm{i}k_{\mathrm{P0}}B_n(\omega,k_{\mathrm{P0}})}{\sqrt{q_{\mathrm{P0}}\sin\theta|w_{\mathrm{P}}''(k_{\mathrm{P0}})|}}\cos\theta\right)\cos(n\varphi)\right] e^{R(\mathrm{i}k_{\mathrm{P0}}\cos\theta - q_{\mathrm{P0}}\sin\theta)-\mathrm{i}\pi/4} \\ u_{R-\mathrm{sv}} = \dfrac{S(\omega)}{n\,!}\left(\dfrac{fr_0}{2}\right)^n \dfrac{1}{4\pi\rho V_{\mathrm{SV}}^2 R}\left[\rho V_{\mathrm{SV}}^2\left(\dfrac{-b'q_{\mathrm{SV0}}F_n(\omega,k_{\mathrm{SV0}})}{\sqrt{q_{\mathrm{SV0}}\sin\theta|w_{\mathrm{SV}}''(k_{\mathrm{SV0}})|}}\sin\theta + \dfrac{\mathrm{i}k_{\mathrm{SV0}}b'F_n(\omega,k_{\mathrm{SV0}})}{\sqrt{q_{\mathrm{SV0}}\sin\theta|w_{\mathrm{SV}}''(k_{\mathrm{SV0}})|}}\cos\theta\right)\cos(n\varphi)\right] e^{R(\mathrm{i}k_{\mathrm{SV0}}\cos\theta - q_{\mathrm{SV0}}\sin\theta)-\mathrm{i}\pi/4} \end{cases} \tag{12}$$

With regard to SH wave:

$$u_{\varphi} = \frac{S(\omega)}{n\,!}\left(\frac{fr_0}{2}\right)^n \frac{1}{4\pi\rho V_{\mathrm{SH}}^2 R}\left[\frac{\rho V_{\mathrm{SH}}^2 q_{\mathrm{SH0}}D_n(\omega,k_{\mathrm{SH0}})\sin(n\varphi)}{\sqrt{q_{\mathrm{SH0}}\sin\theta|w_{\mathrm{SH}}''(k_{\mathrm{SH0}})|}}\right] e^{R(\mathrm{i}k_{\mathrm{SH0}}\cos\theta - q_{\mathrm{SH0}}\sin\theta)-\mathrm{i}\pi/4} \tag{13}$$

With regard to qSV wave:

$$\begin{cases} u_{\theta-\mathrm{sv}} = \dfrac{S(\omega)}{n\,!}\left(\dfrac{fr_0}{2}\right)^n \dfrac{1}{4\pi\rho V_{\mathrm{SV}}^2 R}\left[\rho V_{\mathrm{SV}}^2\left(\dfrac{-\mathrm{i}k_{\mathrm{SV0}}q_{\mathrm{SV0}}F_n(\omega,k_{\mathrm{SV0}})}{\sqrt{q_{\mathrm{SV0}}\sin\theta|w_{\mathrm{SV}}''(k_{\mathrm{SV0}})|}}\cos\theta - \dfrac{-q_{\mathrm{SV0}}^2F_n(\omega,k_{\mathrm{SV0}})}{\sqrt{q_{\mathrm{SV0}}\sin\theta|w_{\mathrm{SV}}''(k_{\mathrm{SV0}})|}}\sin\theta\right)\cos(n\varphi)\right] e^{R(\mathrm{i}k_{\mathrm{SV0}}\cos\theta - q_{\mathrm{SV0}}\sin\theta)-\mathrm{i}\pi/4} \\ u_{\theta-\mathrm{p}} = \dfrac{S(\omega)}{n\,!}\left(\dfrac{fr_0}{2}\right)^n \dfrac{1}{4\pi\rho V_{\mathrm{P}}^2 R}\left[\rho V_{\mathrm{P}}^2\left(\dfrac{-\mathrm{i}k_{\mathrm{P0}}a'q_{\mathrm{P0}}B_n(\omega,k_{\mathrm{P0}})}{\sqrt{q_{\mathrm{P0}}\sin\theta|w_{\mathrm{P}}''(k_{\mathrm{P0}})|}}\cos\theta - \dfrac{-a'q_{\mathrm{P0}}^2B_n(\omega,k_{\mathrm{P0}})}{\sqrt{q_{\mathrm{P0}}\sin\theta|w_{\mathrm{P}}''(k_{\mathrm{P0}})|}}\sin\theta\right)\cos(n\varphi)\right] e^{R(\mathrm{i}k_{\mathrm{P0}}\cos\theta - q_{\mathrm{P0}}\sin\theta)-\mathrm{i}\pi/4} \end{cases} \tag{14}$$

The values of k_{P0}, k_{SV0} and k_{SH0} are derived by calculating the anisotropic steepest-descent solutions for the axial wavenumbers k_{P}, k_{SV} and k_{SH}, respectively. The phase velocities V_{P}, V_{SV}, and V_{SH} correspond to qP, qSV, and SH waves and vary with the radiation angle θ. It is evident that, owing to the coupling between the qP and qSV waves, both the displacement expressions for qP and qSV waves encompass two distinct components, this contrasts significantly with the isotropic scenario. Comprehensive details regarding the anisotropic steepest-descent solutions and the expressions for $w_{\mathrm{P}}''(k_{\mathrm{P0}})$, $w_{\mathrm{SV}}''(k_{\mathrm{SV0}})$ and $w_{\mathrm{SH}}''(k_{\mathrm{SH0}})$ are meticulously outlined in the work of Gu et al. (2023).

Radiant waves propagate outward in a spherical manner, distributing their energy across the surface of a sphere with radius R, encompassing an area of $4\pi R^2$. The energy-flux density of the radiant wave is quantified as the energy conveyed by acoustic waves through a unit area of this spherical surface. Mathematically, the energy flux density of a unit spherical area is expressed as

$$\begin{aligned} E_{\mathrm{rad}} = -\frac{1}{2}\mathrm{Re}\big(&v_{R-\mathrm{P}}^*\sigma_{RR-\mathrm{P}} + v_{R-\mathrm{SV}}^*\sigma_{RR-\mathrm{SV}} + v_{\theta-\mathrm{P}}^*\sigma_{R\theta-\mathrm{P}} \\ &+ v_{\theta-\mathrm{SV}}^*\sigma_{R\theta-\mathrm{SV}} + v_{\varphi-\mathrm{SH}}^*\sigma_{R\varphi}\big) \end{aligned} \tag{15}$$

where $v_{R-\mathrm{P}}^*\sigma_{RR-\mathrm{P}}$, $v_{R-\mathrm{SV}}^*\sigma_{RR-\mathrm{SV}}$, $v_{\theta-\mathrm{P}}^*\sigma_{R\theta-\mathrm{P}}$, $v_{\theta-\mathrm{SV}}^*\sigma_{R\theta-\mathrm{SV}}$ and $v_{\varphi-\mathrm{SH}}^*\sigma_{R\varphi}$ denote the energy flux density for qP-qP, qP-qSV, qSV-qP, qSV-qSV and SH waves.

To determine the complex conjugates of particle velocities in Eq. (15), we substitute Eqs. (12)–(14) into the velocity-displacement relation. This procedure yields the expressions for the particle velocities.

With regard to qP wave:

$$\begin{cases} v_{R-\mathrm{P}} = \dfrac{\mathrm{i}\omega}{4\pi\rho V_{\mathrm{P}}^2 R}\left[\rho V_{\mathrm{P}}^2\left(\begin{array}{l}\dfrac{-q_{\mathrm{P0}}B_n(\omega,k_{\mathrm{P0}})}{\sqrt{q_{\mathrm{P0}}\sin\theta|w_{\mathrm{P}}''(k_{\mathrm{P0}})|}}\sin\theta+\\ \dfrac{\mathrm{i}k_{\mathrm{P0}}B_n(\omega,k_{\mathrm{P0}})}{\sqrt{q_{\mathrm{P0}}\sin\theta|w_{\mathrm{P}}''(k_{\mathrm{P0}})|}}\cos\theta\end{array}\right)\cos(n\varphi)\right]e^{R(\mathrm{i}k_{\mathrm{P0}}\cos\theta-q_{\mathrm{P0}}\sin\theta)-\mathrm{i}\pi/4} \\ v_{R-\mathrm{sv}} = \dfrac{\mathrm{i}\omega}{4\pi\rho V_{\mathrm{SV}}^2 R}\left[\rho V_{\mathrm{SV}}^2\left(\begin{array}{l}\dfrac{-b'q_{\mathrm{SV0}}F_n(\omega,k_{\mathrm{SV0}})}{\sqrt{q_{\mathrm{SV0}}\sin\theta|w_{\mathrm{SV}}''(k_{\mathrm{SV0}})|}}\sin\theta+\\ \dfrac{\mathrm{i}k_{\mathrm{SV0}}b'F_n(\omega,k_{\mathrm{SV0}})}{\sqrt{q_{\mathrm{SV0}}\sin\theta|w_{\mathrm{SV}}''(k_{\mathrm{SV0}})|}}\cos\theta\end{array}\right)\cos(n\varphi)\right]e^{R(\mathrm{i}k_{\mathrm{SV0}}\cos\theta-q_{\mathrm{SV0}}\sin\theta)-\mathrm{i}\pi/4} \end{cases} \tag{16}$$

With regard to SH wave:

$$v_{\varphi} = \frac{\mathrm{i}\omega}{4\pi\rho V_{\mathrm{SH}}^2 R}\left[\frac{\rho V_{\mathrm{SH}}^2 q_{\mathrm{SH0}}D_n(\omega,k_{\mathrm{SH0}})\sin(n\varphi)}{\sqrt{q_{\mathrm{SH0}}\sin\theta|w_{\mathrm{SH}}''(k_{\mathrm{SH0}})|}}\right]e^{R(\mathrm{i}k_{\mathrm{SH0}}\cos\theta-q_{\mathrm{SH0}}\sin\theta)-\mathrm{i}\pi/4} \tag{17}$$

With regard to qSV wave:

$$\begin{cases} v_{\theta-\mathrm{sv}} = \dfrac{\mathrm{i}\omega}{4\pi\rho V_{\mathrm{SV}}^2 R}\left[\rho V_{\mathrm{SV}}^2\left(\begin{array}{l}\dfrac{-\mathrm{i}k_{\mathrm{SV0}}q_{\mathrm{SV0}}F_n(\omega,k_{\mathrm{SV0}})}{\sqrt{q_{\mathrm{SV0}}\sin\theta|w_{\mathrm{SV}}''(k_{\mathrm{SV0}})|}}\cos\theta-\\ \dfrac{-q_{\mathrm{SV0}}^2F_n(\omega,k_{\mathrm{SV0}})}{\sqrt{q_{\mathrm{SV0}}\sin\theta|w_{\mathrm{SV}}''(k_{\mathrm{SV0}})|}}\sin\theta\end{array}\right)\cos(n\varphi)\right]e^{R(\mathrm{i}k_{\mathrm{SV0}}\cos\theta-q_{\mathrm{SV0}}\sin\theta)-\mathrm{i}\pi/4} \\ v_{\theta-\mathrm{p}} = \dfrac{\mathrm{i}\omega}{4\pi\rho V_{\mathrm{P}}^2 R}\left[\rho V_{\mathrm{P}}^2\left(\begin{array}{l}\dfrac{-\mathrm{i}k_{\mathrm{P0}}a'q_{\mathrm{P0}}B_n(\omega,k_{\mathrm{P0}})}{\sqrt{q_{\mathrm{P0}}\sin\theta|w_{\mathrm{P}}''(k_{\mathrm{P0}})|}}\cos\theta-\\ \dfrac{-a'q_{\mathrm{P0}}^2B_n(\omega,k_{\mathrm{P0}})}{\sqrt{q_{\mathrm{P0}}\sin\theta|w_{\mathrm{P}}''(k_{\mathrm{P0}})|}}\sin\theta\end{array}\right)\cos(n\varphi)\right]e^{R(\mathrm{i}k_{\mathrm{P0}}\cos\theta-q_{\mathrm{P0}}\sin\theta)-\mathrm{i}\pi/4} \end{cases} \tag{18}$$

In order to determine the stress components in Eq. (15), we substitute Eqs. (12)–(14) into the strain-displacement relation, yielding the stress components through the application of Hooke's law.

With regard to qP wave:

With regard to qSV wave:

$$\begin{cases} \sigma_{RR-\mathrm{P}} = \dfrac{S(\omega)}{n!}\left(\dfrac{fr_0}{2}\right)^n\dfrac{\cos(n\varphi)}{4\pi R}\left[\dfrac{-c_{11}\omega^2B_n(\omega,k_{\mathrm{P0}})}{V_{\mathrm{P}}^2\sqrt{q_{\mathrm{P0}}\sin\theta|\psi_{\mathrm{P}}''(k_{\mathrm{P0}})|}}\right]e^{R(\mathrm{i}k_{\mathrm{P0}}\cos\theta-q_{\mathrm{P0}}\sin\theta)-\mathrm{i}\pi/4} \\ \sigma_{RR-\mathrm{SV}} = \dfrac{S(\omega)}{n!}\left(\dfrac{fr_0}{2}\right)^n\dfrac{\cos(n\varphi)}{4\pi R}\left[\dfrac{-c_{11}\omega^2b'F_n(\omega,k_{\mathrm{SV0}})}{V_{\mathrm{SV}}^2\sqrt{q_{\mathrm{SV0}}\sin\theta|\psi_{\mathrm{SV}}''(k_{\mathrm{SV0}})|}}\right]e^{R(\mathrm{i}k_{\mathrm{SV0}}\cos\theta-q_{\mathrm{SV0}}\sin\theta)-\mathrm{i}\pi/4} \end{cases} \tag{19}$$

$$\begin{cases} \sigma_{R\theta-\mathrm{SV}} = \dfrac{S(\omega)}{n\,!}\left(\dfrac{fr_0}{2}\right)^n \dfrac{\cos(n\varphi)}{4\pi R}\left[\dfrac{-i\omega^3 c_{44}\sin\theta F_n(\omega,k_{\mathrm{SV0}})}{V_{\mathrm{SV}}^3\sqrt{q_{\mathrm{SV0}}\sin\theta|\psi_{\mathrm{SV}}{}''(k_{\mathrm{SV0}})|}}\right] e^{R(\mathrm{i}k_{\mathrm{SV0}}\cos\theta - q_{\mathrm{SV0}}\sin\theta)-\mathrm{i}\pi/4} \\ \sigma_{R\theta-\mathrm{P}} = \dfrac{S(\omega)}{n\,!}\left(\dfrac{fr_0}{2}\right)^n \dfrac{\cos(n\varphi)}{4\pi R}\left[\dfrac{-ia'\omega^3 c_{44}\sin\theta B_n(\omega,k_{\mathrm{P0}})}{V_{\mathrm{P}}^3\sqrt{q_{\mathrm{P0}}\sin\theta|\psi_{\mathrm{P}}{}''(k_{\mathrm{P0}})|}}\right] e^{R(\mathrm{i}k_{\mathrm{P0}}\cos\theta - q_{\mathrm{P0}}\sin\theta)-\mathrm{i}\pi/4} \end{cases} \tag{20}$$

With regard to SH wave:

$$\sigma_{R\varphi} = \frac{S(\omega)}{n\,!}\left(\frac{fr_0}{2}\right)^n \frac{\sin(n\varphi)}{4\pi R}\left[\frac{c_{66}\omega^2\sin\theta D_n(\omega,k_{\mathrm{SH0}})}{V_{\mathrm{ph-SH}}^2\sqrt{q_{\mathrm{SH0}}\sin\theta|\psi_{\mathrm{SH}}{}''(k_{\mathrm{SH0}})|}}\right] e^{R(\mathrm{i}k_{\mathrm{SH0}}\cos\theta - q_{\mathrm{SH0}}\sin\theta)-\mathrm{i}\pi/4} \tag{21}$$

By substituting Eqs. (19)–(21) and Eqs. (16)–(18) into Eq. (15), we derive the radiated energy flux density E_{rad}. Integrating E_{rad} over a sphere centered on the borehole source with a radius of R, the radiation energy flux is determined in the following

$$W_{\mathrm{rad}}^{\mathrm{m}} = \pi\int_0^{\pi}\left(E_{\mathrm{rad}}^{\mathrm{m}}\cdot R^2\cdot\sin\theta\right)\mathrm{d}\theta, (\mathrm{m} = \mathrm{qP\text{-}qP, qP\text{-}qSV, qSV\text{-}qP, qSV\text{-}qSV\ and\ SH}) \tag{22}$$

where superscripts qP-qP, qP-qSV, qSV-qP, qSV-qSV and SH wave, respectively.

3. Results and analysis

3.1. Verification of anisotropic method in the isotropic formation

Initially, we direct our attention to an isotropic formation (specifically, the Sandstone outlined in Table 1) to establish the validity of the anisotropic formulation in this particular context.

In Fig. 2, we present a comparison between the dispersion curves, energy fluxes of the flexural wave, energy fluxes of radiation waves, and radiation efficiencies. These values are respectively computed using Eqs. (9), (11) and (22) based on the anisotropic method, and the isotropic solution, computed following the approach outlined by Cao et al. (2016). The exact agreement observed between isotropic results (depicted as dots) and anisotropic results (illustrated as solid curves) serves to validate both the formulation and the obtained results.

3.2. The energy flux and radiant efficiency in VTI formation

For the purpose of investigating the impact of formation anisotropy on borehole source excitation, we select Sandstone and Austin Sandstone as representative formations, enabling the illustration of disparities in energy flux and radiant efficiency between isotropic and anisotropic scenarios. Fig. 3 depicts the dispersion curves (calculated using Eq. (9)) and energy fluxes of flexural waves (computed using Eq. (11)) for both isotropic Sandstone and anisotropic Austin Sandstone (formation properties detailed in Table 1). As shown in Fig. 3(a), the velocity of the dispersive flexural mode in Sandstone closely approaches the shear velocity $V_{\mathrm{s}} = \sqrt{\mu/\rho}$ at lower frequencies, where μ represents the formation shear modulus. However, in Austin Sandstone, the phase and group velocities of the mode at low-frequency limits equate to the shear velocity ($V_{\mathrm{s}} = \sqrt{c_{44}/\rho}$) propagating along the axial direction of the borehole. Notably, a minimum group velocity emerges within the medium frequency range, leading to the phenomenon known as the Airy phase. This phase is characterized by the slowest wave propagation and the most pronounced wave energy, corresponding to the peaks observed in the flexural-wave energy flux presented in Fig. 3(b). The energy flux values offer insights into the behavior of flexural waves during transitions between different media. The observed trend of flexural-wave energy fluxes is noteworthy; they exhibit an initial increase followed by a subsequent decrease with rising frequency. For the isotropic case, the energy fluxes reach the peak in the vicinity of 5.4 kHz; however, this frequency shifts to 5.8 kHz for the VTI case. Evidently, formation anisotropy results in a higher peak frequency and a diminished peak value.

Our focus now shifts towards radiant energy fluxes and efficiency in both isotropic and VTI formations. In Fig. 4(a), the impact of anisotropy on the source radiation is evident when compared to the isotropic case. In the Austin Sandstone, five radiation waves are observed, each corresponding to a displacement component as described in Eqs. (12)–(14). The primary components (qP-qP, qSV-qSV, and SH waves) mirror the three radiation waves observed in isotropic Sandstone (P, SV, and SH waves). However, the polarization directions of qP and qSV waves are neither perpendicular nor parallel to the wave propagation directions, leading to the emergence of coupling components (qP-qSV and qSV-qP waves). Notably, the energy flux of SH and qP-qP radiant waves in the VTI situation is greater than their counterparts in isotropic media. Conversely, the peak value of qSV-qSV radiant energy flux is lower

Table 1
The anisotropic parameters and density of the medium.

Medium	c_{11}, GPa	c_{33}, GPa	c_{13}, GPa	c_{44}, GPa	c_{66}, GPa	ρ, kg/m^3
Fluid	2.25	2.25	2.25	–	–	1000
Sandstone	36.8	36.8	12.5	12.2	12.2	2300
Austin Sandstone	36.8	23.4	12.5	9.4	12.167	2300
Iso unconsolidated formation	7.78	7.78	6.74	0.51	0.51	2000
Ani unconsolidated formation	7.78	5.94	5.13	0.41	0.51	2000

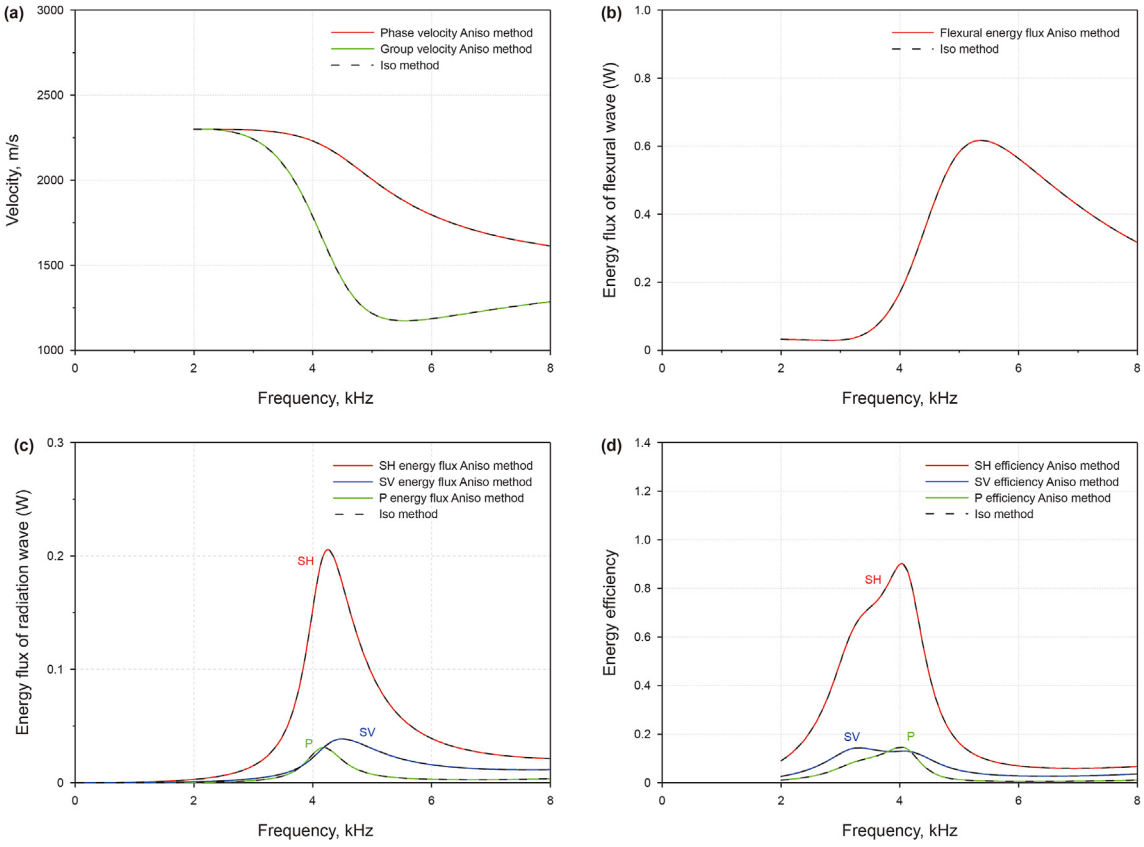

Fig. 2. Comparison of **(a)** dispersion curves, **(b)** energy flux of flexural wave, **(c)** energy fluxes of radiation waves and **(d)** radiation efficiency calculated using isotropic (solid curves) and anisotropic (dots) methods in isotropic Sandstone formation.

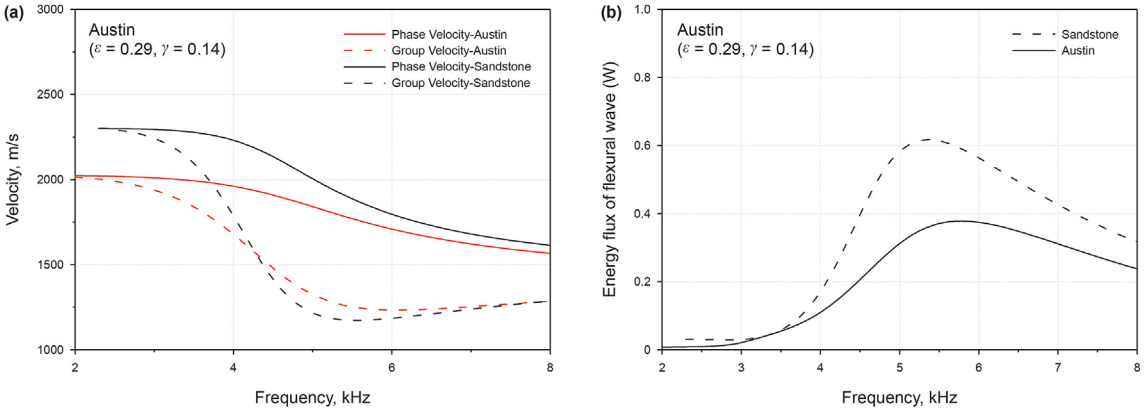

Fig. 3. Comparison of **(a)** dispersion curves and **(b)** energy flux of flexural wave of borehole dipole source in Sandstone and Austin Sandstone.

than its counterpart in isotropic media. Furthermore, the presence of anisotropy causes the flexural-wave energy flux to decrease, while the energy flux of the coupling radiation wave appears. These changes in energy flux highlight the energy conversion between

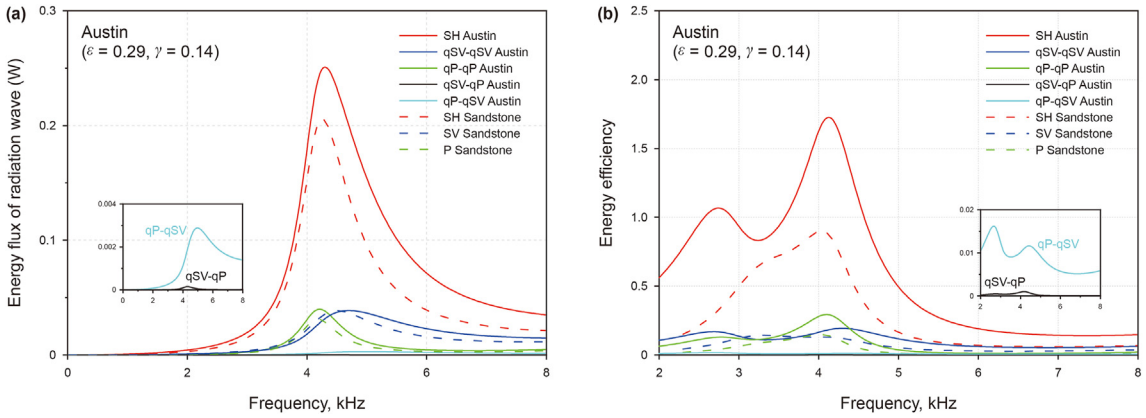

Fig. 4. Comparison of **(a)** energy fluxes of radiation waves and **(b)** radiation efficiencies of borehole dipole source in Sandstone and Austin Sandstone.

different wave components. Additionally, as shown in Fig. 4(a), the energy flux of the qP-qSV wave is notably higher than that of the qSV-qP wave, consistent with the findings obtained by Gu et al. (2023) for the borehole-dipole radiation pattern.

Regarding the radiation efficiency in Fig. 4(b), the SH wave exhibits the highest efficiency in both isotropic and VTI formations, rendering it the most suitable candidate for DSRS. The optimal excitation frequency in the isotropic formation is approximately 4.2 kHz. In contrast, the scenario becomes more intricate in the VTI formation when compared to its isotropic counterpart. There are two peaks for the SH-wave radiation efficiency, the corresponding excitation frequencies are around 2.7 and 4.1 kHz. The presence of a dominant excitation frequency (2.7 kHz) in the low-frequency domain gives the main difference in SH-wave radiation efficiencies between isotropic and anisotropic media.

3.3. The effect of elastic parameters on energy flux and radiant efficiency

Sensitivity analysis holds a paramount role in exploring the impact of elastic parameters on energy distribution. Kazei and Alkhalifah (2019) employ a scattering atlas to elucidate the responsiveness of scattered wavefields to distinct anisotropic parameters. To attain deeper insights into radiation-energy characteristics concerning formation anisotropy, we simulate the influence of Thomson anisotropic parameters ε and γ (Thomsen, 1986) and five elastic parameters on radiation energy flux. Varied perturbations in the anisotropic parameters yield diverse radiation energy flux patterns, consequently enabling the radiation energy flux atlas to effectively capture the sensitivity of radiation energy to these anisotropic parameters.

We consider a Sandstone background, as detailed in Table 1, and systematically perturb ε and γ independently, with each value ranging from 0 to 0.1. The resultant variations are depicted in the energy flux sensitivity plot presented in Fig. 5. For each parameter perturbation, we calculate the energy flux within the frequency range of 3.0–6.0 kHz. The color intensity in the plot corresponds to the magnitude of the energy flux. Analysis of the sensitivity plots reveals distinct trends. Specifically, we observe that SH wave radiation is essentially insensitive to perturbations of ε, with the energy flux exhibiting small changes at various frequencies. In contrast, the perturbation of γ significantly affects SH wave radiation, indicating the pronounced sensitivity of SH wave radiation to shear wave anisotropy.

Subsequently, we systematically perturb five anisotropic elastic parameters independently in the same manner, each ranging from 0% to 15%. These perturbations serve to increase c_{11} and c_{66}, respectively, or decrease c_{33}, c_{13}, and c_{44}, respectively. The resulting variations are depicted in the energy flux sensitivity plot presented in Fig. 6. Specifically, we observe that the SH-wave radiation remains largely insensitive to variations in c_{13} and c_{33}, with the energy flux exhibiting minimal changes at individual frequencies. While the influence of c_{11} is relatively minor, notable impacts are evident when considering c_{44} or c_{66}, both of which markedly affect SH-wave radiation. Notably, we identify a discernible enhancement in the energy flux peak, accompanied by a slight upward shift in the corresponding frequency, particularly in cases where c_{44} decreases or c_{66} increases. This observation underscores the substantial sensitivity of SH-wave radiation to shear-wave anisotropy and is consistent with the conclusions obtained in Fig. 5.

It is noteworthy to mention that when elastic waves radiate from a borehole source into a VTI formation, both compressional and shear wave anisotropies manifest simultaneously within the wavefield. Consequently, a more judicious approach involves analyzing energy flux sensitivity through concurrent reductions in c_{33} and c_{44}. This strategy yields a more pronounced enhancement in peak values and frequency shifts, as depicted in Fig. 6. In the subsequent sections, we delve into an exploration of the impact of formation anisotropy on energy flux and radiant efficiency, achieved by simultaneous perturbations of c_{33} and c_{44} within the range of 0%–15% (the corresponding ranges of Thomsen anisotropy parameters ε, γ and δ are 0–0.088, 0–0.088 and 0–0.062, respectively).

To study the influence of anisotropy on guided waves, we employ the calculation of flexural wave energy flux (Eq. (11)), simultaneously perturbing c_{33} and c_{44} within the range of 0%–15%. Owing to the presence of a cut-off frequency for guided wave, we establish our excitation frequency spanning from 2 to 8 kHz for the analytical study. As depicted in Fig. 7, the graphical representation showcases the variations in energy flux concerning both frequency and perturbed anisotropic parameters. In the isotropic scenario, where a 0% reduction is considered, the flexural wave energy flux attains a peak magnitude at a frequency of 5.4 kHz. Particularly, as formation anisotropy is progressively augmented, a conspicuous decline in the peak value becomes evident, concomitant with a concurrent elevation in the corresponding peak frequency. Under the conditions of a 15% reduction in both c_{33} and c_{44}, the energy flux achieves its maximum amplitude, representing half of the isotropic counterpart's value, and is observed at 5.9 kHz. This trend signifies a significant impedance imposed on the propagation of flexural waves due to the anisotropic characteristics engendered by sedimentary structures. Moreover, this phenomenon suggests the

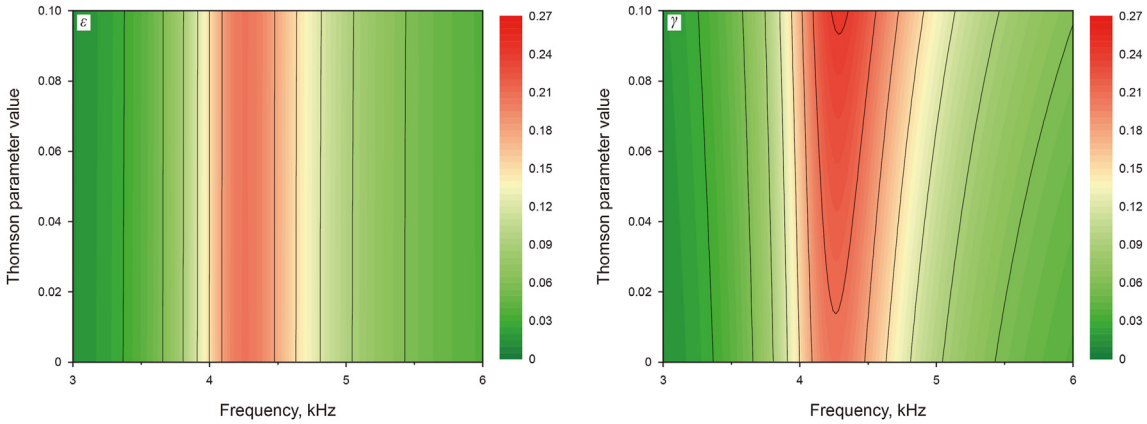

Fig. 5. The radiation atlas describes the sensitivity of SH-wave energy flux to Thomson anisotropic parameters and excited frequency.

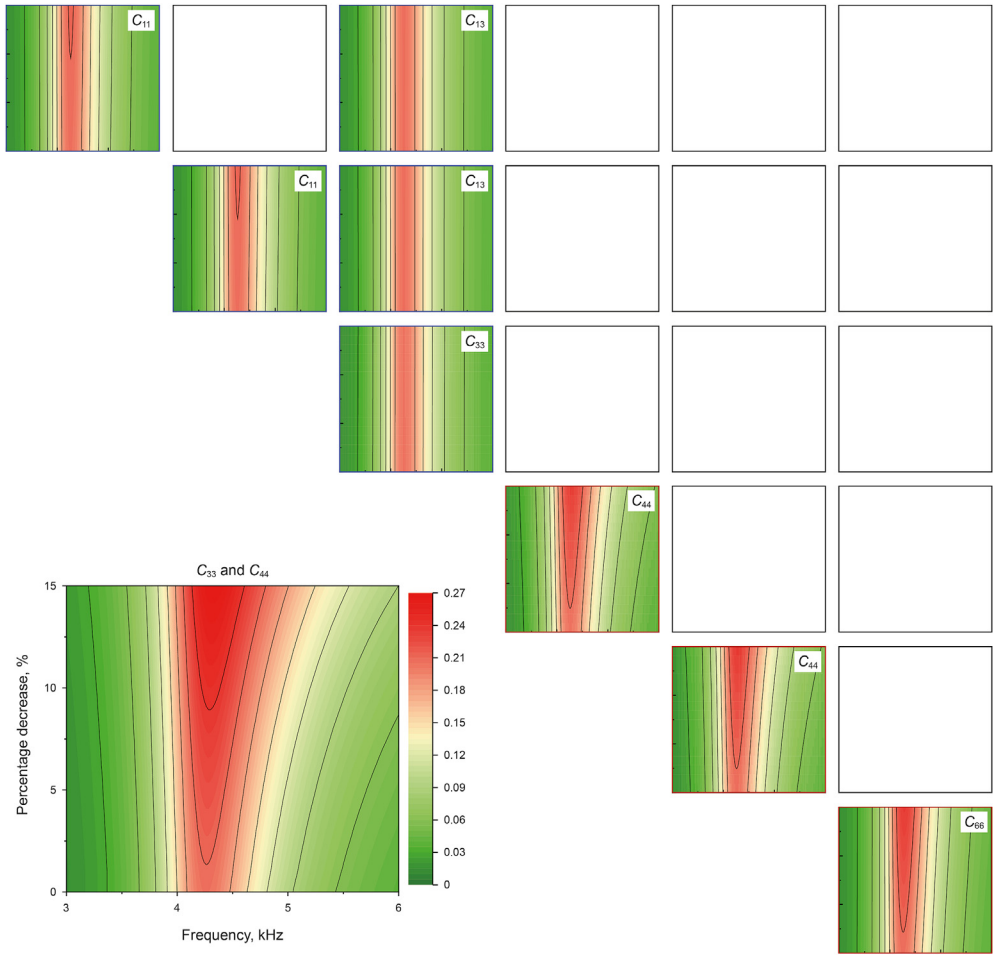

Fig. 6. The radiation atlas describes the sensitivity of SH-wave energy flux to anisotropic parameters and excited frequency.

plausible occurrence of mode conversion from guided waves to radiated waves, consistent with the principle of energy conservation.

Fig. 8 illustrates the impact of formation anisotropy on the energy fluxes of qP and qSV radiation waves. In the majority of studied wave modes, a reduction in c_{33} and c_{44} enhances wave anisotropy, consequently leading to increased energy fluxes in wave pairs such as qP-qP (Fig. 8(a)), qP-qSV (Fig. 8(b)), and qSV-qP (Fig. 8(c)). However, an exception arises with the qSV-qSV wave (Fig. 8(d)), where an increment in wave anisotropy corresponds to a gradual decline in energy flux. Notably, this behavior mirrors the phenomenon observed in the flexural wave discussed in Fig. 7. This similarity arises due to their analogous polarization directions and shared contribution of wave energy to mode conversion within VTI media. Within the frequency range of dipole-logging, both the qP-qP wave and qSV-qP wave exhibit peak frequencies that remain

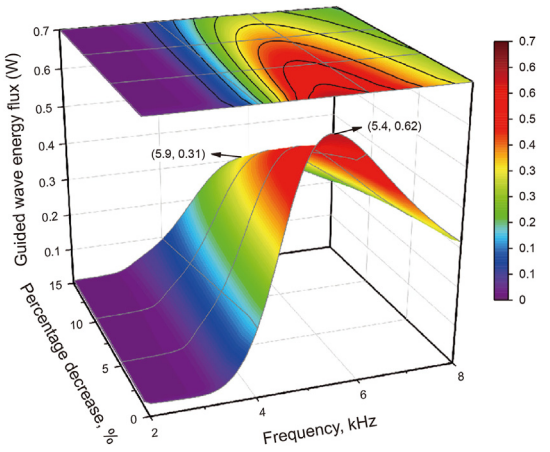

Fig. 7. Flexural wave energy flux varies with frequency and anisotropic parameters perturbation with a percentage decrease of c_{33} and c_{44} ranging from 0% to 15%.

unaltered by anisotropy, displaying narrow peaks. In contrast, the presence of anisotropy induces a slight frequency shift towards higher frequencies for qSV-qSV and qP-qSV waves. With respect to coupling components, the energy flux variation of qP-qSV wave surpasses that of qSV-qP wave. Particularly, under the conditions of a 15% decrease in both c_{33} and c_{44}, the peak value for qP-qSV wave exceeds that of qSV-qP wave by an order of magnitude. This observation highlights the heightened sensitivity of the qSV component, relative to the qP component, to formation anisotropy.

Fig. 9 presents the depiction of SH-wave energy flux variation concerning both frequency and anisotropic parameters. Unlike the SV-wave case illustrated in Fig. 8, the SH wave exhibits a distinct behavior characterized by a pure mode, where its energy flux escalates concomitantly with an increase in formation anisotropy. This disparity underscores a noteworthy contrast, revealing that the SH wave possesses the capacity to radiate energy into the VTI formation more effectively when its particle motion aligns with the bedding plane, in contrast to its behavior when perpendicular to the bedding plane. Comparatively, in relation to qP and qSV waves, the SH wave attains the most prominent peak value of energy flux. This observation indicates the dominance of the SH mode within the DSRS.

For a more detailed investigation into the impact of anisotropy on SH-wave radiation, we explore the variations of SH-wave energy flux density (calculated using $E_{\mathrm{rad}}^{\mathrm{SH}} = -\frac{1}{2}\mathrm{Re}(v_{\varphi}^{*}\sigma_{R\varphi})$ according to Eq. (15)), with respect to frequency and radiation angle. This analysis encompasses both isotropic conditions (c_{33} and c_{44} reduced by 0%) and anisotropic media (c_{33} and c_{44} reduced by 15%), as depicted in Fig. 10(a) and (b) correspondingly. Examining the energy flux density profiles in isotropic and anisotropic formations reveals a discernible correlation between the dominant radiation frequency and radiation angle. Notably, both figures exhibit symmetry with respect to a 90° angle line, and the dominant frequency experiences a decrement as the radiation angle progresses from 0° to 90°. In essence, when the SH-wave radiates perpendicular to the borehole axis, the dominant frequency notably diminishes compared to scenarios where the wave propagates along the borehole.

As observed earlier, the presence of formation anisotropy amplifies SH-wave energy flux. This observation indicates that within the entire range of radiation angles, the energy flux density in

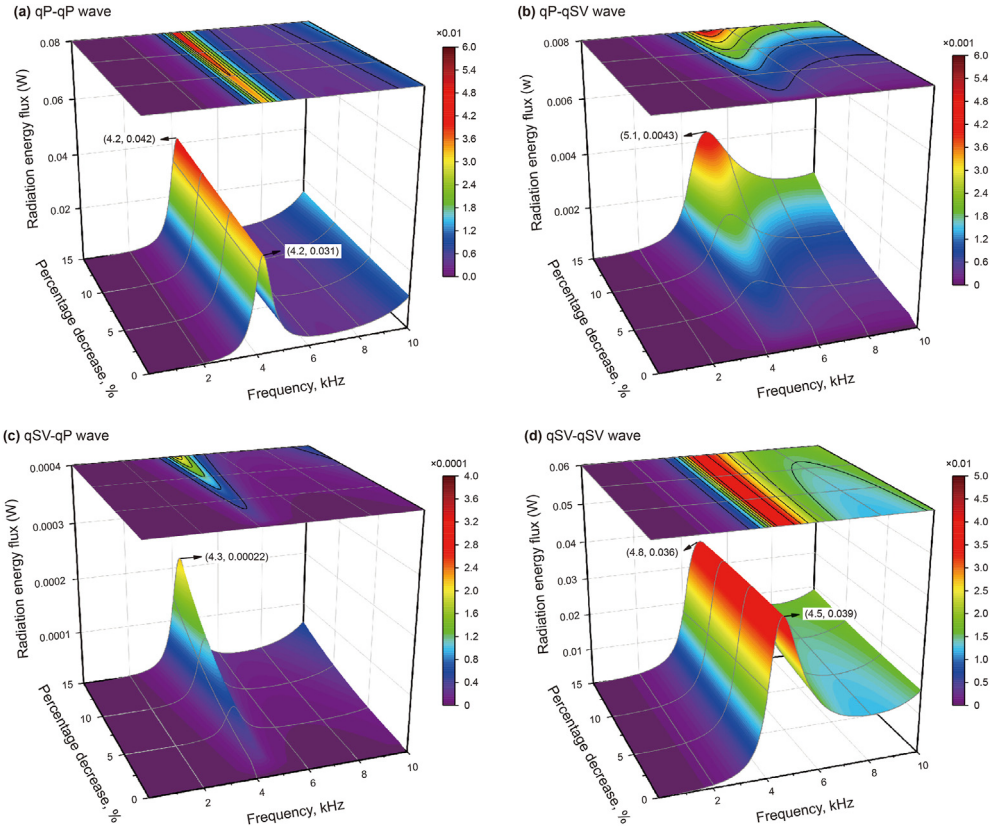

Fig. 8. Radiation energy fluxes of **(a)** qP-qP, **(b)** qP-qSV, **(c)** qSV-qP and **(d)** qSV-qSV wave vary with frequency and anisotropic parameters perturbation with a percentage decrease of c_{33} and c_{44} ranging from 0% to 15%.

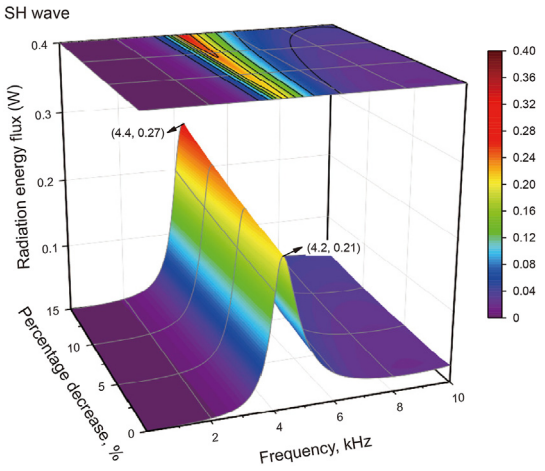

Fig. 9. Radiation energy flux of SH wave varies with frequency and anisotropic parameters perturbation with a percentage decrease of c_{33} and c_{44} ranging from 0% to 15%.

anisotropic media surpasses that of its isotropic counterpart. This discrepancy is attributed to the reduction in c_{33} and c_{44}. However, a more comprehensive analysis is warranted to evaluate energy characteristics across diverse radiation angles. Fig. 10(c) juxtaposes SH-wave energy flux density between anisotropic (solid curve) and isotropic (dashed curve) scenarios, focusing on a radiation angle of 90°. While no significant frequency shift is apparent, a noticeable increase in the peak value for the anisotropic case aligns with expectations. Fig. 10(d) mirrors Fig. 10(c) with the exception of a radiation angle set at 10°, thereby examining the scenario of SH wave radiation nearly along the borehole axis. Upon scrutiny, the results unveil intriguing insights. Anisotropy induces an augmented energy flux density at high-frequency ranges; however, intriguingly, a decrement is observed in the context of low-frequency cases. This phenomenon underscores that anisotropy's influence on the increase of SH-wave energy is nuanced, bearing a close interrelation with the radiation angle.

It is imperative to mention that the evaluation of radiation energy flux outside the borehole cannot be directly applied to optimize excitation frequencies for DSRS, primarily due to the omission of significant guided waves. Hence, the assessment of the dominant excitation-frequency band necessitates consideration of radiation efficiency, a parameter delineating the capacity of the borehole source to convey elastic energy into the formation. To ascertain this, we divide the radiation energy fluxes of qP and qSV waves, depicted in Fig. 8, by the flexural wave energy flux presented in Fig. 7. This approach gives the variations in radiation efficiencies for qP and qSV waves with respect to frequency and anisotropic parameters within the 2–8 kHz frequency band, as illustrated in Fig. 11.

Upon examination, it becomes evident that all radiation efficiencies exhibit two prominent peaks, characterized as low-frequency and high-frequency peaks, in the presence of formation anisotropy. However, under isotropic conditions, the radiation efficiency of the qP-qP wave manifests a solitary peak, while that of the qP-qSV and qSV-qP waves registers as zero. Across the majority of considered wave modes, the magnitude of both low- and high-frequency peaks escalates with increasing anisotropy. Notably, this trend is disrupted for the low-frequency peaks associated with qP-qP and qSV-qSV waves, where the magnitude initially rises and subsequently diminishes with increasing anisotropy. Another intriguing observation is the amplification of low-frequency peaks within the qSV components (qP-qSV and qSV-qSV waves),

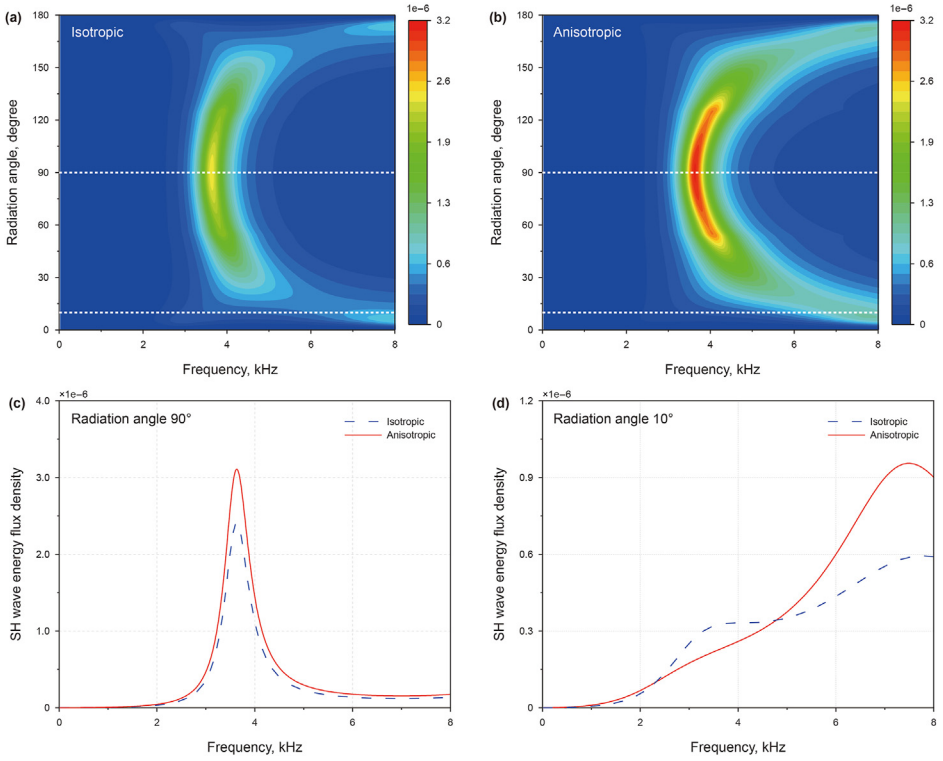

Fig. 10. Comparison of SH-wave energy flux density varies with frequency and radiation angle in **(a)** isotropic and **(b)** anisotropic formations. The SH-wave energy flux density of anisotropic (the solid curve) and isotropic (the dashed curve) scenarios is also plotted, separately, at the radiation angles of **(c)** 90° (perpendicular to the borehole) and **(d)** 10° (nearly along the borehole).

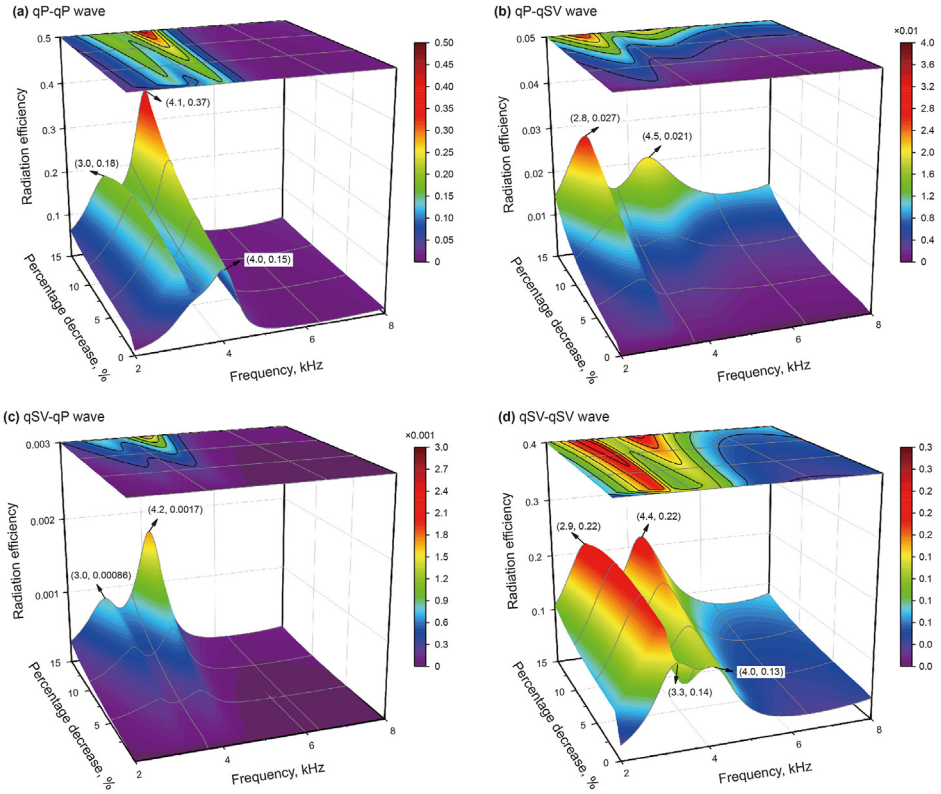

Fig. 11. Radiation efficiencies of **(a)** qP-qP, **(b)** qP-qSV, **(c)** qSV-qP and **(d)** qSV-qSV waves vary with frequency and anisotropic parameters perturbation with a percentage decrease of c_{33} and c_{44} ranging from 0% to 15%.

surpassing their high-frequency counterparts. Conversely, the peak amplitudes of the qP components (qP-qP and qSV-qP waves) show a contrary trend. Throughout the frequency band, the variation in dominant excitation frequency attributed to anisotropy remains a salient feature.

Utilizing the same computational approach and parameters outlined in Fig. 11, we present the depicted variations of SH radiation efficiency concerning frequency and anisotropic parameters in Fig. 12. Notably, within the context of the SH wave, heightened anisotropy yields an augmented magnitude of the high-frequency peak, as well as a shift of this peak towards higher frequencies.

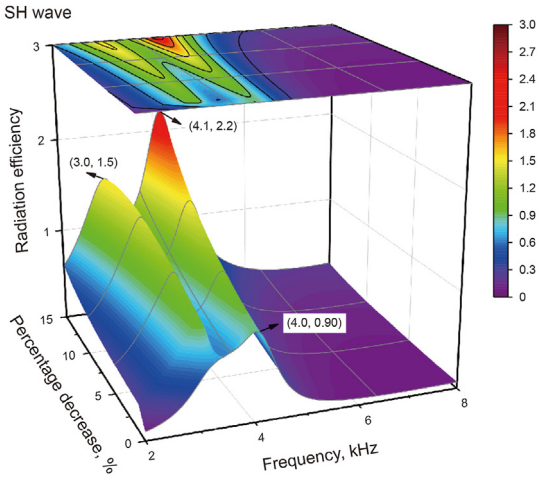

Fig. 12. SH-wave radiation efficiency varies with frequency and anisotropic parameters perturbation with a percentage decrease of c_{33} and c_{44} ranging from 0% to 15%.

Conversely, the low-frequency peak displays an initial amplitude increment, succeeded by a decrement with escalating anisotropy. This low-frequency peak similarly shifts towards lower frequencies. A comparative analysis of the radiation efficiencies depicted in Figs. 11 and 12 underscores a pivotal observation. Despite the excitation of five radiated wave modes by the dipole source, the SH wave emerges as the optimal choice for precise borehole reflection imaging due to its elevated radiation efficiency. A key disparity between the SH radiation efficiency of isotropic and anisotropic medium lies in the manifestation of a low-frequency peak within anisotropic media. This observation serves as a fundamental underpinning for designing the center frequency of the excited borehole source and optimizing the frequency band of the employed bandpass filter.

4. Field data examples

Given the results presented above, one can design the acoustic excited system of a logging source and optimize the bandpass filter band for borehole reflection imaging. In the following, we apply our method to field data processing and provide evidence of the presence of a low-frequency peak in anisotropic media. The imaging results with different frequency bands from the anisotropic formation will be compared with those from the isotropic formation to demonstrate the validity of our results.

Fig. 13 shows the detailed imaging results for the 45 m depth interval across a limestone formation of Bohai Bay Basin. The borehole is drilled using water-based mud with a density of 1000 kg/m^3 and an acoustic velocity of 1500 m/s. Panel 1 displays the borehole caliper (CAL) and density (DEN) curves across the formation. In panel 2, the compressional (DTP) and shear (DTS) slowness curves are presented, with smooth curves indicating a

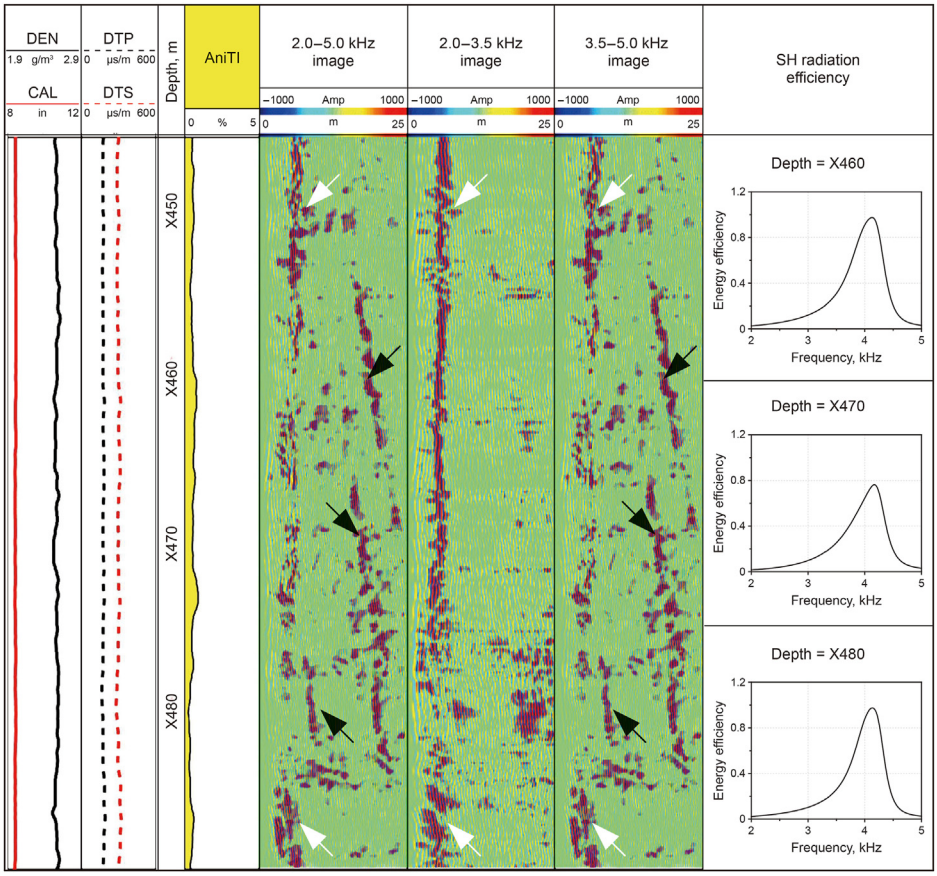

Fig. 13. Field example of using radiation efficiency (see panel 7) to explain the different frequency bands image of 2.0–5.0 kHz (Panel 4), 2.0–3.5 kHz (Panel 5), and 3.5–5.0 kHz (Panel 6) in isotropic formation (Panel 3 displays a very low shear anisotropy value). Panel 1 displays the CAL and DEN curves. Note that the radiation efficiency is calculated using the DTP and DTS curves in Panel 2, the density curve, and the anisotropy value.

stable borehole condition. Panel 3 gives the shear anisotropy value extracted from the dipole data by the borehole flexural-wave inversion method. As described by Xu et al. (2017), the VTI properties of formation significantly influence the flexural-wave dispersion, and the sensitivity peaks align with observed peaks in the flexural wave energy flux, corresponding to the Airy phase of flexural waves. The inversion method involves calculating the theoretical flexural wave dispersion curve specific to the VTI formation and utilizing it to fit the measured wave dispersion data. This enables the simultaneous determination of vertical and horizontal shear wave velocities, from which we can obtain the shear anisotropy value.

One can see that the shear-wave anisotropy value over the section is less than 0.5% which can be regarded as an isotropic case. As described by Tang and Patterson (2009), an effective preprocessing procedure including wavenumber filtering, frequency band-pass filtering, etc, is generally implemented before migration and imaging to suppress low-frequency guide waves and extract the reflection signals. We perform a comparative study of the imaging results in different frequency bands by adjusting the frequency filtering parameters while keeping other preprocessing and migration parameters unchanged. In our approach, we employ an integrated framework to suppress borehole guide waves with substantial amplitude by cascading parametric array wave estimation method, *f-k* filtering and median filtering. The transmitter-receiver array data is utilized to separate up- and down-going reflection waves based on the apparent slowness difference between reflection and direct waves, respectively. In the case of acoustic logging data, the shear wave slowness obtained from logging measurements conveniently constructs the velocity model. After migrating the array reflection data through the Kirchhoff method, the acoustic reflection data are projected onto the 2D domain for geological structure imaging. The resulting image for the frequency bands of 2.0–5.0 kHz (Panel 4), 2.0–3.5 kHz (Panel 5), and 3.5–5.0 kHz (Panel 6) reveal the difference of using borehole acoustic data with different frequency bands. Compared with the imaging result with a low-frequency band (2.0–3.5 kHz), which displays the dominant direct waves residue (as labeled by the white arrows), the migration image with a high-frequency band (3.5–5.0 kHz) shows several well-defined, high-angle reflectors (as labeled by the black arrows) around the borehole, in addition, the imaging result with a full-frequency band (2.0–5.0 kHz) displayed as a reference. This phenomenon can be well-explained with the SH radiation efficiency (Panel 7) calculated from the parameter curves in Panels 1–3. Although the peak values of SH radiation efficiency at the three typical depth positions are different from each other, their corresponding dominant excitation frequencies are all around 4.2 kHz, as contained in the high-frequency and full-frequency bands. Thus the reflection events are visualized in those two frequency band results but disappear in the low-frequency band result, which indicates that radiation efficiency can be used to design filter bands to improve imaging quality.

To compare with the imaging results from the isotropic formation, another example concerns a 40 m depth shaly-sand formation from Shengli Oil Field as shown in Fig. 14. The CAL and DEN curves are displayed in panel 1. The borehole is also drilled with water-

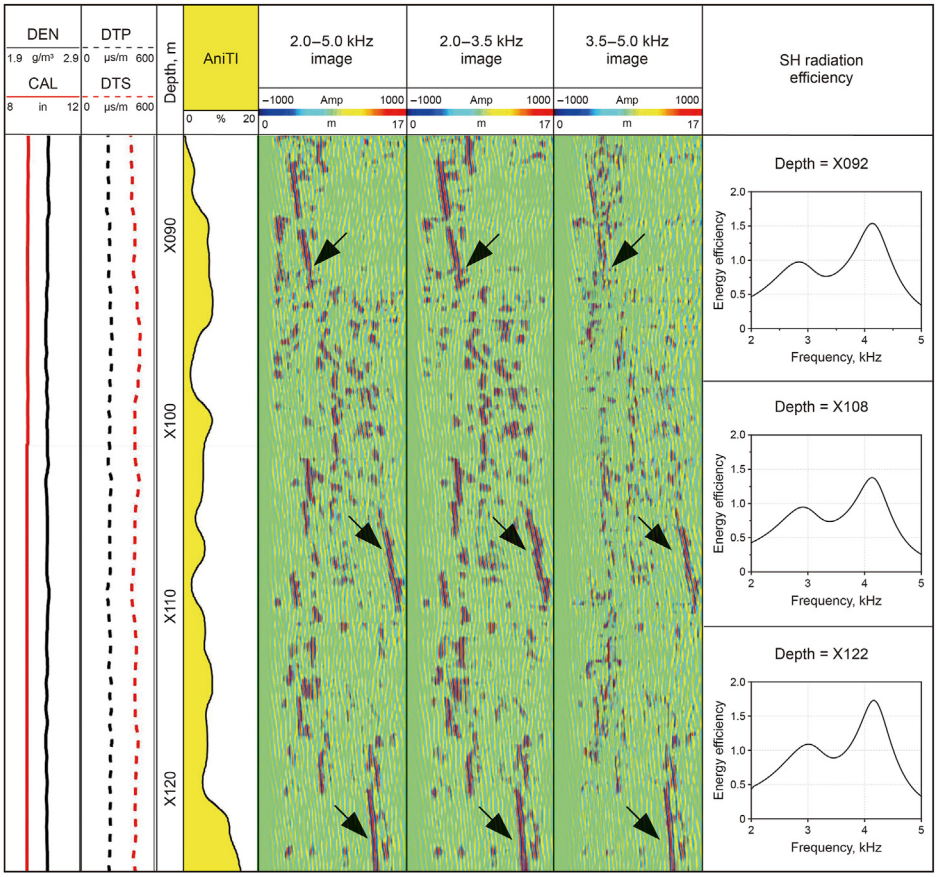

Fig. 14. Field example of using radiation efficiency (see panel 7) to explain the different frequency bands image of 2.0–5.0 kHz (Panel 4), 2.0–3.5 kHz (Panel 5), and 3.5–5.0 kHz (Panel 6) in anisotropic formation (Panel 3 displays a significant shear anisotropy value). Panel 1 displays the CAL and DEN curves. Note that the radiation efficiency is calculated using the DTP and DTS curves in Panel 2, the density curve, and the anisotropy value.

based mud. One can see from panel 2 that the DTP and DTS curves show a good anticorrelation with density value. A superior dipole data is recorded for the entire depth interval, giving a dependable shear anisotropy value of 10% on average in panel 3. The considerable anisotropy values, as picked from the depth of interest, are 7.78%, 5.85%, and 13.24%, respectively, demonstrating the borehole penetrates an acoustically anisotropic formation, for which our SH-wave radiation efficiencies (Panel 7) of anisotropic formation can be used to analyze the different frequency bands imaging results (Panels 4, 5 and 6). A notable characteristic is that, compared with the invisible reflectors in the isotropic low-frequency band (2.0–3.5 kHz) imaging results, the reflection events are visualized clearly in low-frequency, high-frequency and full-frequency bands in the anisotropic case, indicating that there is a low-frequency peak in addition to a high-frequency peak in anisotropic formation. The two frequency peaks around 2.9 and 4.2 kHz of anisotropic SH-wave radiation efficiency in Panel 7 confirm this interpretation. It is noteworthy that, for a clear characterization of the reflectors, images from various frequency bands are individually normalized based on their respective maximum values. This approach enhances the comparability of imaging across different frequency bands. However, this separate normalization leads to a decrease in imaging amplitude in the high-frequency band compared to the low-frequency band. Without normalization, the situation is reversed, aligning with the observation that the high-frequency peak value exceeds that of the low-frequency peak in radiation efficiency.

5. Discussion

Most sedimentary strata exhibit horizontal lamination, rendering VTI medium the prevalent anisotropic model in borehole geophysics. The presence of anisotropic stratigraphic environments introduces complexity to the distribution of acoustic energy in the borehole. The results shown in Fig. 4(a) confirm that SH wave is the predominant mode for dipole acoustic reflection imaging in fast formation. However, further discussion is warranted for shallow,

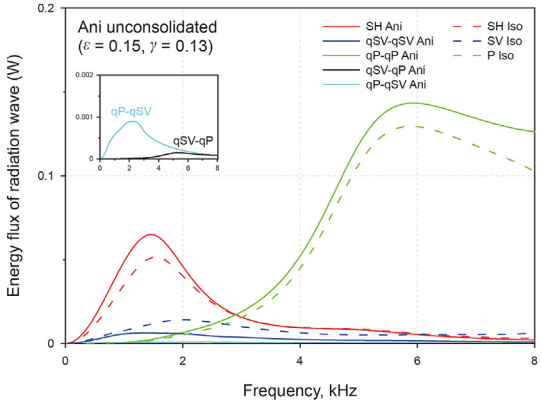

Fig. 15. Comparison of energy fluxes of radiation waves of borehole dipole source in isotropic and anisotropic unconsolidated formations.

very slow formations.

Fig. 15 provides a comparative analysis of the radiation energy flux from a borehole dipole acoustic source in isotropic and anisotropic unconsolidated formations (the parameters are given in Table 1). As we can see, the energy fluxes of SH and qP-qP radiation waves in anisotropic unconsolidated conditions surpass their counterparts in isotropic media. The peak value of the qSV-qSV energy flux is lower than that in the isotropic medium. In contrast to the fast formation scenario, the SH wave in unconsolidated formation has a low-frequency energy flux peak at 1.5 kHz, with pronounced logging noise often present near this frequency band. Particularly noteworthy is that in the acoustic logging band (2–5 kHz), the energy flux of the qP-qP wave surpasses that of the SH wave, suggesting that the dipole P wave, rather than the S wave, dominates reflection imaging in unconsolidated formations.

To further discuss the preceding analysis results, we perform continuous acoustic reflection logging simulations across the Austin Sandstone and anisotropic unconsolidated formation using the analytical modeling method (Gu et al., 2023). A 20° inclined reflector is positioned at a radial distance of 8–12 m from the borehole axis. The reflector models in Fig. 16(a) and (b) are set up as oil- or gas-filled fractures with a stiffness of 50 GPa/m, and the reflection coefficients are calculated using slip interface theory (Schoenberg, 1980). The reflector models in Fig. 16(c) and (d) are set up as formation interfaces, with the formations on either side of the interface being Austin Sandstone or anisotropic unconsolidated formation (see Table 1). The reflection coefficients at the interface are calculated using the Zoeppritz equation (Li et al., 2017). In Fig. 16(a), a variable density plot of the SH wave data (Panel 1) and the qP and qSV wave data (Panel 2) in the Austin Sandstone formation is presented, with amplitudes normalized to the maximum value. It is evident that qP-qP, qSV-qSV, and converted waves exhibit relatively weak signals and mutual interference, while the SH wave emerges as the most prominent and clear signal. The SH wave imaging result (Panel 3) is consistent with the fracture model parameters, demonstrating the significance of SH wave for reflection imaging in conventional formation. Conversely, in the presence of an unconsolidated formation surrounding the borehole, Fig. 16(b) illustrates notably higher amplitudes of qP-qP waves, allowing clear imaging of the fracture using qP-qP wave (Panel 3) Additionally, the qSV-qP wave demonstrates a considerable amplitude compared to the SH wave. Notably, due to the finite

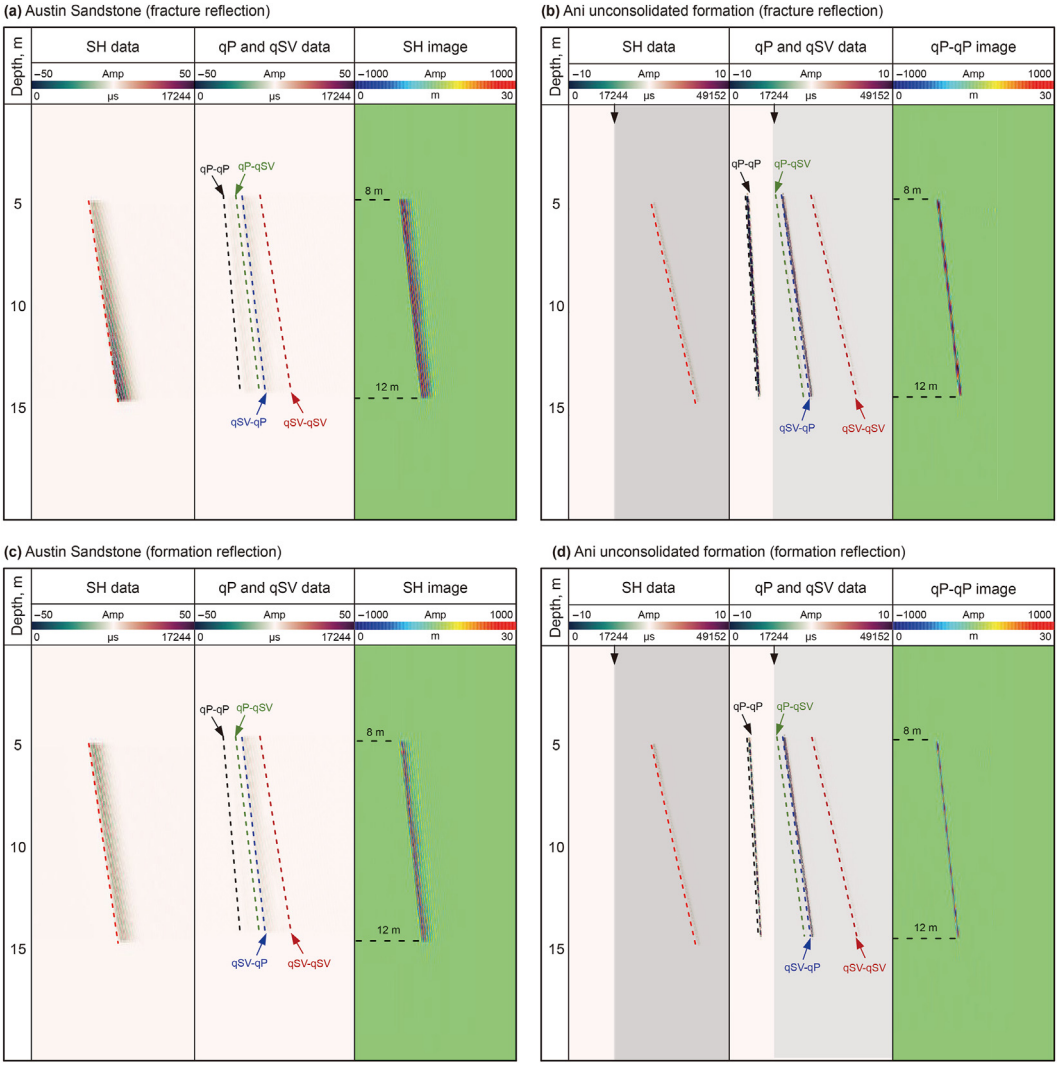

Fig. 16. Comparison of synthetic reflection data and imaging results from **(a)** Austin Sandstone fracture model, **(b)** anisotropic unconsolidated formation fracture model, **(c)** Austin Sandstone formation interface model with anisotropic unconsolidated formation on the other side of the interface, and **(d)** anisotropic unconsolidated formation interface model with Austin Sandstone on the other side of the interface.

logging recording time of 17244 μs, other reflected waves, except qP-qP waves, from the very slow formation are challenging to record. Therefore, the qP-qP wave proves advantageous for imaging the reflector in very slow formation scenarios. The formation-reflected wavefield and imaging results in Fig. 16(c) or (d) are consistent with those obtained from the fracture reflection simulations in Fig. 16(a) or (b), respectively. However, the reflected waves from the fractures are stronger in amplitude and more clearly imaged than those from the formation interface because a considerable amount of the elastic wave energy propagates through the formation interface, while most of the elastic wave energy is reflected to the borehole receiver by the oil- or gas-filled fractures.

6. Conclusion

The presence of formation anisotropy can significantly affect the energy distribution from a borehole dipole source. The effective theoretical approach implemented in this paper is performed to analyze the influences of anisotropy on DSRS from the energy fluxes and radiation efficiencies. Our result extends the previous work for the isotropic formation and shows that, although there are five radiated wave modes excited by the dipole source, the SH wave remains the optimal choice for reflection surveys in fast formations due to its superior radiation efficiency. Conversely, the qP-qP wave exhibits advantages over S waves in unconsolidated formations. The dominant excitation-frequency band of the SH wave widens within the VTI formation. Furthermore, the VTI formation yields two peaks in SH-wave radiation efficiency. The presence of dominant excitation frequency in the low-frequency domain gives the main difference in SH-wave radiation efficiencies between isotropic and anisotropic media. The field data for DSRS validate the key role of the dominant excitation-frequency band. Our results can guide the design and measurement methods of the DSRS, which could have extensive application prospects for unconventional oil and gas exploration.

CRediT authorship contribution statement

Xi-Hao Gu: Writing – review & editing, Writing – original draft, Validation, Methodology, Investigation, Formal analysis, Data curation, Conceptualization. **Fan-Tong Kong:** Software, Investigation, Formal analysis. **Yuan-Da Su:** Validation, Resources, Investigation, Data curation. **Xiao-Ming Tang:** Writing – review & editing, Validation, Supervision, Resources, Project administration, Methodology, Investigation, Funding acquisition, Formal analysis, Data curation, Conceptualization.

Declaration of competing interest

The authors declare that they have no known competing financial interests or personal relationships that could have appeared to influence the work reported in this paper.

Acknowledgement

The authors thank the reviewers for their comments and suggestions that helped to improve the manuscript. This work was supported by the National Natural Science Foundation of China (grant No. 42074137, 42204126, 41821002, U21B2064); Laoshan National Laboratory Science and Technology Innovation Project (grant No. LSKJ202203407); China Scholarship Council State Scholarship Fund (202206450061).

Appendix A

Elements of N_{ij} and b_i

The elements of N_{ij} and b_i are given below:

$$b_1 = \varepsilon_n \left[\frac{n}{a}K_n(fa) - fK_{n+1}(fa)\right]$$

$$b_2 = -\varepsilon_n \rho_f \omega^2 K_n(fa)$$

$$b_3 = 0$$

$$b_4 = 0$$

$$N_{11} = -\frac{n}{a}I_n(fa) - fI_{n+1}(fa)$$

$$N_{12} = (1 + \mathrm{i}ka')\left[\frac{n}{a}K_n(q_P a) - q_P K_{n+1}(q_P a)\right]$$

$$N_{13} = \frac{n}{a}K_n(q_{SH} a)$$

$$N_{14} = (b' + \mathrm{i}ka)\left[\frac{n}{a}K_n(q_{SV} a) - q_{SV} K_{n+1}(q_{SV} a)\right]$$

$$N_{21} = \rho_f \omega^2 I_n(fa)$$

$$N_{22} = \left[c_{11}(1 + \mathrm{i}ka')q_P^2 + c_{13}\left(-k^2 - \mathrm{i}ka' q_P^2\right)\right]K_n(q_P a) + 2c_{66}(1 + \mathrm{i}ka')\left[\frac{n(n-1)}{a^2}K_n(q_P a) + \frac{q_P}{a}K_{n+1}(q_P a)\right]$$

$$N_{23} = 2nc_{66}\left[\frac{n-1}{a^2}K_n(q_{SH} a) - \frac{q_{SH}}{a}K_{n+1}(q_{SH} a)\right]$$

$$N_{24} = \left[c_{11}(b' + \mathrm{i}k)q_{SV}^2 + c_{13}\left(-k^2 b' - \mathrm{i}kq_{SV}^2\right)\right]K_n(q_{SV} a) + 2c_{66}(b' + \mathrm{i}k)\left[\frac{n(n-1)}{a^2}K_n(q_{SV} a) + \frac{q_{SV}}{a}K_{n+1}(q_{SV} a)\right]$$

$$N_{31} = 0$$

$$N_{32} = 2nc_{66}(1 + \mathrm{i}ka')\left[\frac{1-n}{a^2}K_n(q_P a) + \frac{q_P}{a}K_{n+1}(q_P a)\right]$$

$$N_{33} = -c_{66}\left\{\left[\frac{2n(n-1)}{a^2} + q_{SH}^2\right]K_n(q_{SH} a) + \frac{2q_{SH}}{a}K_{n+1}(q_{SH} a)\right\}$$

$$N_{34} = 2nc_{66}(b' + \mathrm{i}k)\left[\frac{1-n}{a^2}K_n(q_{SV} a) + \frac{q_{SV}}{a}K_{n+1}(q_{SV} a)\right]$$

$$N_{41} = 0$$

$$N_{42} = c_{44}\left[2\mathrm{i}k - a'\left(q_P^2 + k^2\right)\right]\left[\frac{n}{a}K_n(q_P a) - q_P K_{n+1}(q_P a)\right]$$

$$N_{43} = \frac{\mathrm{i}nkc_{44}}{a}K_n(q_{SH} a)$$

$$N_{44} = c_{44}\left[2ikb' - \left(k^2 + q_{SV}^2\right)\right]\left[\frac{n}{a}K_n(q_{SV}a) - q_{SV}K_{n+1}(q_{SV}a)\right]$$

where a denotes the radius of the borehole, ε_n denotes the Neuman's factor, f and q denote, separately, the radial wavenumbers of the fluid and formation, and subscripts SH, P and SV denote an SH wave and the coupled qP and qSV waves.

References

Cao, J.J., Tang, X.M., Su, Y.D., et al., 2016. Radiation efficiency of a multipole acoustic source in a fluid–filled borehole. Chin. J. Geophys. 59 (1), 89–99. https://doi.org/10.1002/cjg2.20216 (in Chinese).

Cheng, L., Che, X.H., Qiao, W.X., et al., 2023. 3D trajectory inversion of an adjacent well using scattered P-wave. Petrol. Sci. 20 (2), 857–865. https://doi.org/10.1016/j.petsci.2023.02.024.

Dong, W., Toksöz, M.N., 1995. Borehole seismic-source radiation pattern in transversely isotropic media. Geophysics 60 (1), 29–42. https://doi.org/10.1190/1.1443759.

Fang, X.D., Fehler, M.C., Cheng, A., 2014. Simulation of the effect of stress-induced anisotropy on borehole compressional wave propagation. Geophysics 79 (4), D205–D216. https://doi.org/10.1190/geo2013-0186.1.

Gu, X.H., Tang, X.M., Su, Y.D., 2021. Delineating a cased borehole in unconsolidated formations using dipole acoustic data from a nearby well. Geophysics 86 (5), D139–D147. https://doi.org/10.1190/geo2020-0570.1.

Gu, X.H., Tang, X.M., Su, Y.D., et al., 2023. Elastic wave radiation and reception of a borehole dipole source in a vertically transverse isotropic formation. Geophysics 88 (2), D177–D191. https://doi.org/10.1190/geo2022-0174.1.

Han, T., Gurevich, B., Fu, L.Y., et al., 2020. Combined effects of pressure and water saturation on the seismic anisotropy in artificial porous sandstone with aligned fractures. J. Geophys. Res. Solid Earth. 125 (1), e2019JB019091. https://doi.org/10.1029/2019JB019091.

He, X., Hu, H.S., 2009. Borehole flexural modes in transversely isotropic formations: low-frequency asymptotic velocity. Geophysics 74 (4), E149–E158. https://doi.org/10.1190/1.00V7413.

Hei, C., Qi, X., Li, Z., 2023. Evaluation of the downhole hydraulic fracturing using single-well shear wave scattering imaging-modeling and field applications. Waves Random Complex 1–13. https://doi.org/10.1080/17455030.2023.2226238.

Hirabayashi, N., Leaney, W.S., 2019. Wavefield separation for borehole acoustic reflection survey using parametric decomposition and waveform inversion. Geophysics 84 (4), D151–D159. https://doi.org/10.1190/geo2018-0330.1.

Ji, Y., He, X., Chen, H., et al., 2021. Acoustic fields for monopole logging while drilling with an eccentric collar. Geophysics 86 (2), D43–D63. https://doi.org/10.1190/geo2019-0744.1.

Kazei, V., Alkhalifah, T., 2019. Scattering radiation pattern atlas: what anisotropic elastic properties can body waves resolve? J. Geophys. Res. Solid Earth 124 (3), 2781–2811. https://doi.org/10.1029/2018JB016687.

Kong, F., Xu, H., Gu, X., et al., 2023. Denoising method of borehole acoustic reflection image using convolutional neural network. Geoenergy Sci. Eng. 226, 211761. https://doi.org/10.1016/j.geoen.2023.211761.

Lee, S.Q., Chen, M., Gu, X.H., et al., 2019. Application of four-component dipole shear reflection imaging to interpret the geological structure around a deviated well. Appl. Geophys. 16 (3), 291–301. https://doi.org/10.1007/s11770-019-0778-x.

Li, C., Chen, H., He, X., et al., 2021. Identifying reflector azimuth from borehole multicomponent cross-dipole acoustic measurement. Geophysics 86 (6), D201–D214. https://doi.org/10.1190/geo2020-0460.1.

Li, J.X., Innanen, K.A., Tao, G., et al., 2017. Wavefield simulation of 3D borehole dipole radiation. Geophysics 82 (3), D155–D169. https://doi.org/10.1190/geo2016-0145.1.

Li, Z., Lee, S.Q., Qi, Q., et al., 2022. Investigation of through-casing borehole acoustic reflection imaging with a dipole source: modeling and field application. J. Nat. Gas Sci. Eng. 105, 104715. https://doi.org/10.1016/j.jngse.2022.104715.

Liu, J., Zhou, Y., Cui, Z., et al., 2019. Multipole borehole acoustic field in a transversely isotropic medium induced by stress. J. Acoust. Soc. Am. 146 (2), 1290–1301. https://doi.org/10.1121/1.5122974.

Schoenberg, M., 1980. Elastic wave behavior across linear slip interfaces. J. Acoust. Soc. Am. 68 (5), 1516–1521. https://doi.org/10.1121/1.385077.

Tang, W., Tan, M., Cao, H., et al., 2024. Numerical simulation and characteristic analysis of remote detection acoustic reflection imaging logging of near-borehole fracture and vuggy reservoirs. IEEE T Geosci. Rem. 62, 1–12. https://doi.org/10.1109/TGRS.2023.3338856.

Tang, X.M., Cheng, C.H., 2004. Quantitative Borehole Acoustic Methods. Elsevier Science Publishing, Amsterdam.

Tang, X.M., Glassman, H., Patterson, D., 2008. Single-well acoustic imaging in anisotropic formations. Geophysics 73 (4), D11–D16. https://doi.org/10.1190/1.2907522.

Tang, X.M., Gu, X.H., Su, Y.D., 2019. Theoretical analysis and field data application of through-casing dipole shear-wave imaging. J. China Univ. Pet. Nat. Sci. 43 (5), 65–72. https://doi.org/10.3969/j.issn.1673-5005.2019.05.007.

Tang, X.M., Patterson, D., 2009. Single-well S-wave imaging using multicomponent dipole acoustic-log data. Geophysics 74 (6), WCA211–WCA223. https://doi.org/10.1190/1.3227150.

Thomsen, L., 1986. Weak elastic anisotropy. Geophysics 51 (10), 1954–1966. https://doi.org/10.1190/1.1442051.

Wang, H., Tao, G., Shang, X.F., 2015. A method to determine the strike of interface outside of borehole by monopole borehole acoustic reflections. J. Pet. Sci. Eng. 133, 304–312. https://doi.org/10.1016/j.petrol.2015.05.025.

Wei, Z., Tang, X., Cao, J., 2019. Acoustic radiation and reflection of a logging-while-drilling dipole source. Geophys. J. Int. 219 (1), 108–128. https://doi.org/10.1093/gji/ggz193.

Winbow, G.A., 1991. Borehole stresses created by downhole seismic sources. Geophysics 56 (7), 1055–1057. https://doi.org/10.1190/1.1443114.

Xu, J., Liu, Q.H., Hu, H., et al., 2021. Simulation of borehole acoustic wavefields in fractured media by combining the spectral-element method and linear-slip model. Geophysics 86 (5), D177–D192. https://doi.org/10.1190/geo2020-0840.1.

Xu, S., Tang, X.M., Su, Y.D., et al., 2017. Determining formation S-wave transverse isotropy from borehole flexural-wave dispersion data. Geophysics 82 (2), D47–D55. https://doi.org/10.1190/geo2016-0223.1.

Zeng, F.Q., Li, C., 2022. Theoretical dispersion curves for borehole real-valued wave modes in vertically transverse isotropic formations. Petrol. Sci. 19 (6), 2649–2662. https://doi.org/10.1016/j.petsci.2022.04.011.

Zhao, T., Che, X., Qiao, W., et al., 2023. Borehole azimuthal acoustic imaging using 3D spatial scanning: application in acoustic detection of nearby wells. Geophysics 88 (2), D131–D145. https://doi.org/10.1190/geo2022-0376.1.